Unveiling and optimizing interface properties of NiFe_2O_4/BaTiO_3 heterostructures

Haowen Lin, Cristian Mocuta, Rémi Arras, Céline Blaess, Brice Sarpi, Philippe Ohresser, Hélène Magnan, Jean-Baptiste Moussy, Cindy Lynn Rountree, Antoine Barbier

Unveiling and optimizing interface properties of $NiFe_2O_4/BaTiO_3$ heterostructures

Haowen Lin[1,2], Cristian Mocuta[2], Rémi Arras[3], Céline Blaess[1,2], Brice Sarpi[4], Philippe Ohresser[2], Hélène Magnan[1], Jean-Baptiste Moussy[1], Cindy L. Rountree[1], Antoine Barbier[1]*

[1]Université Paris-Saclay, CEA, CNRS, SPEC, 91191, Gif-sur-Yvette, France

[2]Synchrotron SOLEIL, L'Orme des Merisiers Saint-Aubin, BP 48, 91192 Gif sur Yvette Cedex, France

[3]CEMES, Université de Toulouse, CNRS, 29 rue Jeanne Marvig, F-31055 Toulouse, France

[4]Diamond Light Source, Chilton, Didcot, Oxfordshire, UK

[*]Email: antoine.barbier@cea.fr

Abstract:

In this study, we investigate the properties, with a special focus on the magnetic attributes, of $NiFe_2O_4$ (NFO)/$BaTiO_3$ (BTO) multiferroic heterostructures, examining individual layer thicknesses ranging from 3 to 12 nm. X-ray diffraction reveals that as BTO thickness

increases, NFO transfers from a non-strained cubic lattice to a compressive strained tetragonal lattice. In contrast, thicker NFO layers introduce enhanced tensile stresses on the BTO layer, counteracting the compressive strain originating from the $SrTiO_3$ (STO) substrate. Piezoresponse force microscopy demonstrates that polarization switching voltage escalates with increasing BTO layer thickness. Through X-ray magnetic circular dichroism measurements coupled with multiplet theory, we elucidate variations in magnetic moments and ionic distributions within the NFO layers. Remarkably, a larger BTO thickness is associated with a chemical reduction of Fe ions in NFO layer, indicative of increased oxygen vacancies, which is induced by the increasing compressive strain as evidenced by first-principles calculations. Thinner NFO layers showed increased tetrahedral (T_d) site vacancies and oxygen vacancies in concomitant with reduced magnetic moments, which can be optimized by either increasing NFO thickness or through air annealing at 450 °C. Combining the ionic distribution variation with in-plane lattice parameter evolution during growth, we postulated that the reduced magnetic moments originate from a 2-3 nm antiferromagnetic rock salt NiO/FeO formed at the beginning of NFO growth, while the air annealing restores the magnetism by oxidizing and arranging the NiO/FeO into spinel NFO under synergistic effect of oxygen and heat. Air annealing at moderate temperature appears as a very efficient method to restore the magnetization of ultra-thin layers of NFO, allowing to overcome a major drawback for these compounds which hampers its utilization in spintronics applications so far.

Keywords: NiFe2O4, BaTiO3, Multiferroics, Magnetic dead layer, Epitaxial growth, Synchrotron radiation

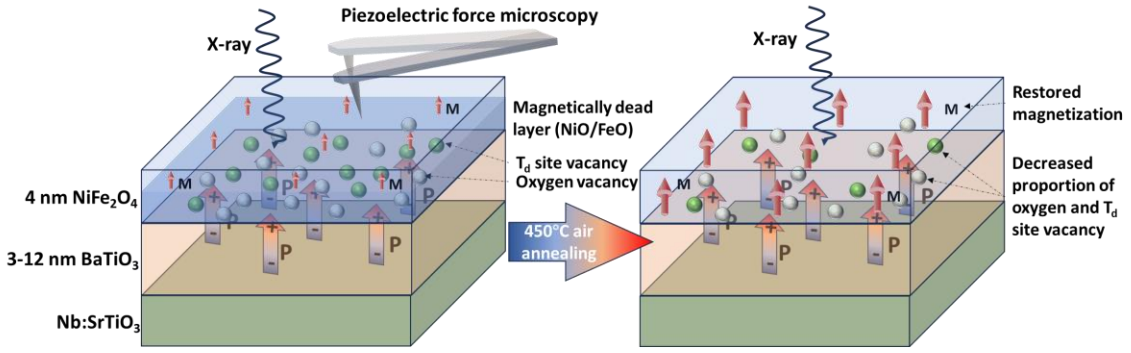

1. Introduction

The escalating demand for energy-efficient computing and storage solutions has propelled extensive research into innovative material systems and devices. Among these materials, multiferroics, combing multiple ferroic properties (e.g., ferroelectricity, ferromagnetism, ferroelasticity and ferrotoroidicity), is a pivotal candidate for next-generation storage and logic devices. These systems combine the advantages of non-volatility, thanks to the stability of the magnetization, and energy-efficiency, through the electric-field manipulation. They have therefore led to innovative devices such as electric-field-controlled magnetic random-access memories[1] and magnetoelectric spin-orbit logic devices[2]. Given the scarcity of room-temperature, stable, single-phase multiferroic materials[3,4], artificial multiferroic systems - which combine different ferroic properties across multiple phases - emerge as a reliable and effective approach. There are different routes of creating artificial multiferroic composites, including particulate composites[5], self-assembled composites[6,7], and multilayer heterostructures[8,9]. Multiferroic heterostructures, in particular, provide a platform to investigate the physical attributes of each component and their interrelations. This aids in the fundamental research into deciphering the intricate interplay of ferroic properties within the system.

In the present work, we study $NiFe_2O_4$ (001) / $BaTiO_3$ (001) multiferroic thin films system deposited on Nb doped $SrTiO_3$ (001) substrate, with perovskite $BaTiO_3$ (BTO) providing ferroelectricity and spinel $NiFe_2O_4$ (NFO) introducing magnetic order. Barium titanate is a notable lead-free displacive ferroelectric, recognized for its high permittivity, room temperature ferroelectricity, and enhanced ferroelectricity in strained layers[10,11]. Within typical BTO (001) epitaxial layer, the epitaxial in-plane strain from the substrate leads to the polarization of BTO aligning along the [001] tetragonal axis. Interface and surface effects will greatly influence the stabilization of polarization in thin films[12]. The spinel ferrite NFO is a soft ferrimagnet characterized by its large resistivity, high Curie temperature for magnetic long range ordering, low anisotropy and notably high permeability, which bolsters magnetoelectric coupling[13]. The coupling between the ferromagnetic and ferroelectric layers hinges predominantly on their interface, where strain, spin and charge coincide[14]. As device miniaturization necessitates using thinner layers, understanding this ferromagnetic/ferroelectric interface becomes increasingly paramount. To our knowledge, no prior systematic study has been conducted on the NFO/BTO interface. Moreover, the mechanism of low magnetization at interface and its associated curing method in multiferroic heterostructures remain elusive.

To address these issues, this study examines the evolution of the ferroic properties in a series of samples combining various layer thickness (the BTO thicknesses, θ_{BTO}, were varied from 3 to 12 nm and those of NFO layers, θ_{NFO}, from 4 to 12 nm). Strain and ferromagnetic properties in the thin multilayers were probed using synchrotron-based X-ray diffraction and X-ray absorption spectroscopy, respectively. Ferroelectricity was evaluated *via* microscopic piezoelectric force microscopy. Intriguingly, the increase of

BTO thickness amplifies the compressive strain imposed on NFO layer, introduces chemical reduction in the NFO layer, and slightly improve the magnetization in the NFO layer. Conversely, the reduction of NFO layer aids in screening the depolarization field, thereby stabilizing the polarization in the BTO layer. However, detrimental very low magnetization is observed in thin NFO layer samples showing the presence of a magnetically dead (or non-magnetic) layer at the interface in the thin film regime. Detailed analyses of valence and site distribution variations within the NFO layer, combined with in-plane lattice parameter variations during growth, lead us to conclude that the nature of this magnetically dead layer is an intermediate antiferromagnetic rock salt NiO/FeO layer formed during NFO deposition. We demonstrate that this magnetically dead layer can be cured through the synergistic effects of oxygen and heat, which reoxidize and rearrange the layer into ferrimagnetic NFO.

2. Experimental Details:

Film Growth:

The Nb:$SrTiO_3$ (Nb:STO) substrates were first pre-annealed in air at 900°C prior to epitaxy for recrystallization to remove polish-induced defects in the surface layer. Subsequently, the substrate was positioned into the Molecular Beam Epitaxy (MBE) chamber and annealed at 450°C for 1h to facilitate outgassing in vacuum and next exposed to a high brilliance oxygen plasma (350 W radiofrequency (RF) power) for 1.5h of surface cleaning. The deposition of the oxide layer is fulfilled with the evaporation of each metal constituent from respective high purity (99.999%) source materials (Ba, Ti, Ni and Fe in present work), commercially obtained from Goodfellow Cambridge Ltd, in dedicated Knudsen cells and the oxidation *via* the oxygen plasma exposure (350 W). The evaporation

rate of metal constituents is optimized for each layer to ensure superior crystalline quality and a correct stoichiometric ratio. The crystalline quality was monitored in real-time by reflection high-energy electron diffraction (RHEED). Auger electron spectroscopy and X-ray photoemission spectroscopy were employed *in situ* to crosscheck the stoichiometry after sample elaboration. X-ray reflectivity is used to determine the relationship between film thickness and deposition time. Further details regarding the epitaxial growth can be found in our previous publications [15–17].

Transmission Electron Microscopy:

High-resolution transmission electron microscopy (HRTEM) was used to access microstructures in real space. Cross-sections of the specimens were prepared using focused ion beam (FIB). The HRTEM observations were performed with a Hitachi I2TEM, while FIB experiments utilized a Helios NanoLab600i.

X-ray Diffraction:

X-ray diffraction (XRD) measurements were realized at the DiffAbs beamline at the SOLEIL synchrotron. The X-rays utilized in the XRD experiments were monochromatic (bandpass of $\Delta E/E \sim 10^{-4}$), with an energy of 9.96 keV. Two 50 nm rhodium-coated Si single crystal mirrors were employed to effectively reject higher harmonics X-rays by a cumulated factor of about 10^{-6}. The beam size of the X-ray was about 200 × 250 μm^2 (FWHM, vertical × horizontal), and the photon flux at the focal spot reached several 10^{12} ph/s.

For capturing the XRD signal, we used a 0D detector (photomultiplier) combined with slits that provided an angular opening of approximately 0.03 × 0.3° (Vertical × Horizontal). The measurement is achieved through scanning the sample (incident angle) and the

detector (scattering angle) in symmetric configuration (θ - 2θ) to access momentum transfer values along the direction perpendicular to the surface of the sample (*i.e.* along the 00L direction). For XRD measurement concerning mapping in reciprocal space, we employed an area detector (hybrid pixels, XPAD model s140) [18–20], consisting of an array of 560 × 240 pixels (130 μm pitch, and gapless). We mounted the 2D detector on the diffractometer's detector circles, allowing it to be positioned around the sample. This setup enabled us to capture a significant angular range in a single image/measurement, approximately 11 × 4° (2θ × ψ, respectively, representing the Bragg scattering angle and polar elevation).

X-ray Spectroscopy:

X-ray absorption spectroscopy (XAS) and X-ray Magnetic Circular Dichroism (XMCD) experiments took place at the DEIMOS beamline at SOLEIL synchrotron. The beam size was 800 × 800 μm^2 with a photon energy resolution of 100 meV. For most sample measurements, the magnetic field was produced by a water-cooling electromagnet with a maximum 1 T magnetic field. Exception was for two particular samples, one 4 nm NFO/4.5 nm BTO and one 7 nm NFO/9 nm BTO, in as-deposited and air-annealed conditions, for which the magnetic field was produced by a superconducting magnet applying a magnetic field up to 5 T along the beam direction. The X-ray beam and magnetic field are both perpendicular to the sample surface. The absorption intensity was acquired using total-electron-yield (TEY) detection mode. XAS spectra are recorded using fully circularly polarized X-rays provided by an Apple-II HU52 undulator. Magnetization curves are recorded using EMPHU65 helical undulator at 10Hz polarization flipping rate. Isotropic XAS spectra is calculated by the average of XAS spectra of opposite circular polarization. XMCD spectra is obtained by first calculating the differences of XAS of opposite circular

polarization and then normalizing the differences by dividing the edge jump of the isotropic XAS.

Scanning Probe Microscopy:

Atomic force microscopy (AFM) and Piezoresponse force microscopy (PFM) imaging were conducted using a Bruker Nanoscope V Dimension ICON microscope. For AFM imaging, SCANAYST air tips in the Peak-Force QNM mode detailed the samples' topography. PFM measurements employed SCM-PIT-V2 tips (with Pt-Ir conductive coating). Both AFM and PFM measurements utilized a DAFMCH tip holder.

First-principles Calculations:

Ab initio calculations based on the density functional theory (DFT) were performed using the VASP code[21,22] with the projector augmented wave (PAW) method[23], and a cut-off energy of 600 eV. The exchange–correlation energy was calculated thanks to the functional proposed by Perdew, Burke, and Ernzerhof and revised for solids (GGA-PBESol)[24] with a Hubbard (+U) correction and $U_{\text{eff}} = (U - J)$ parameters of 4.0 eV for Fe and 2.5 eV for Ni atoms. To calculate the effects of a neutral oxygen vacancy, we employed the same approach as our former publication[25], where we used a 1 × 1 × 1 supercell described by a conventional cubic cell of 8 formula units (f.u.) of $NiFe_2O_4$ (i.e. 56 atoms in total) and the most stable Fe/Ni cation distribution corresponding to the perfectly inverse spinel structure with the space group 91-$P4_122$.

3. Results

Epitaxial NFO over epitaxial BTO thin films with BTO thickness θ_{BTO} = 3, 6, 9, 12 nm and NFO thickness θ_{NFO} = 4, 12 nm were grown on the Nb doped $SrTiO_3$(001) substrate by oxygen plasma assisted molecular beam epitaxy (OA-MBE)[15,26], with growth parameters detailed in experimental section. Well contrasted RHEED streaks observed throughout the entire growth process attest to the good crystal quality of each layer, as demonstrated in Fig. 1a. The comparison of the RHEED patterns between the film and the substrate, combined with the 90° azimuthal periodicity in the RHEED patterns, confirms a cube-on-cube epitaxial growth with c-axis out-of-plane orientation for both BTO on the Nb:STO(001) substrate and NFO atop BTO layers. The appearance, after 20 min of growth, of doubled spaced streaks during the NFO growth implies that NFO is growing in a manner such that one NFO cube aligns with four BTO cubes — two along each crystallographic direction. This observation corresponds well with the lattice parameter relationship between the two layers, the NFO ferrite lattice parameter being slightly larger than the double of the BTO one.

HRTEM images further confirm the good crystallinity of these layers, as showcased in Fig. 1b. Using the AFM, we measured the topography for each layer thickness combination (Fig. S1). The terrace-like morphology is indicative of a sequential layer-by-layer growth. As illustrated by the curve in Fig. 1c, the root mean square roughness values span from 0.4 nm to 1 nm, underscoring a smooth 2D epitaxial growth. It is worth noting that samples with θ_{NFO} = 12 nm present a higher surface roughness than their 4 nm thick counterparts. However, intriguingly, an incremental increase in θ_{BTO} does not consistently result in higher roughness.

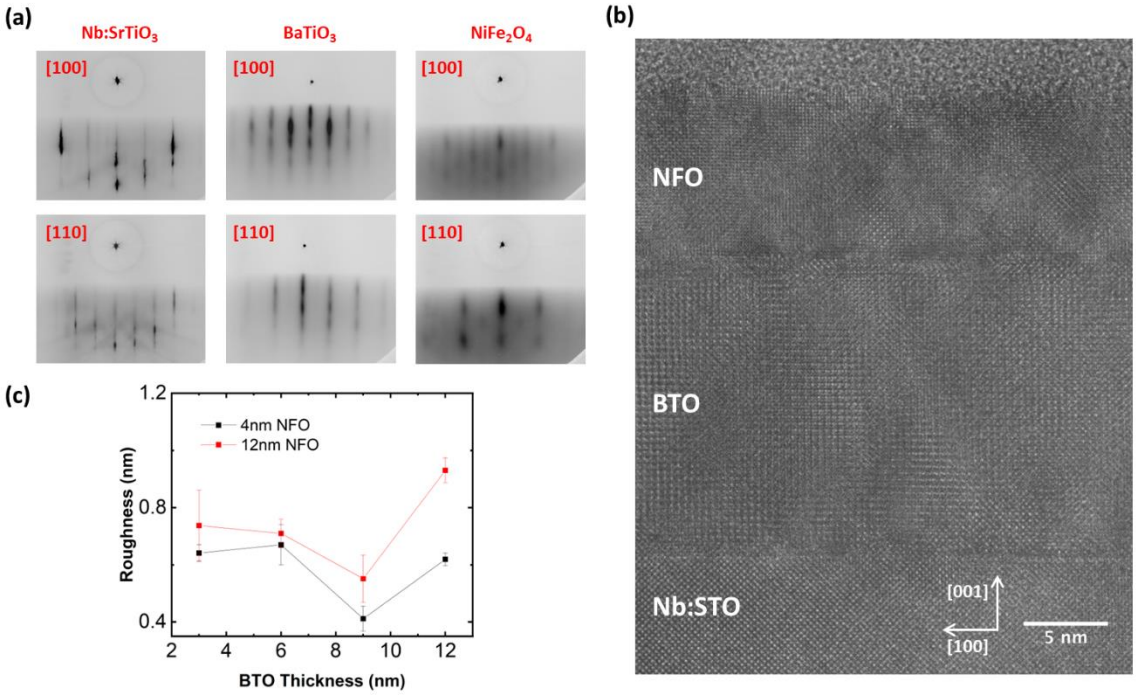

Figure 1. Structural Characterization of layers. (a) *In-situ* RHEED images of the NFO/BTO/Nb:STO heterostructures observed during epitaxial growth, (b) High-resolution TEM images of a 9 nm/17 nm NFO/BTO film on Nb:STO(001) (c) Root mean square roughness of sample surfaces measured by AFM as a function of BTO thickness

Structural properties

At room temperature, bulk perovskite BTO possesses a tetragonal crystal structure, with in and out of plane lattice parameters a_{BTO} = 3.992 Å and c_{BTO}= 4.036 Å respectively[27]. In contrast, STO has a cubic crystal structure with a_{STO} = 3.905 Å[28]. Consequently, the lattice mismatch between BTO and the substrate, determined *via* the formula $(a_{film}-a_{subs})/a_{subs}$, is +2.2%. This signifies an in-plane compressive stress exerted on the BTO film by the substrate. Meanwhile, bulk NFO is characterized by a spinel cubic structure with a_{NFO} = 8.339 Å[29]. Since the lattice parameter of NFO is nearly twice as big as that of BTO and

STO, one NFO cube grows on four BTO/STO cells, and the lattice mismatch between NFO and BTO is thus $(a_{NFO}/2\text{-}a_{BTO})/a_{BTO}$ = +4.45%, while that between NFO and STO is +6.77%. Hence, theoretically NFO shall exhibit in-plane compressive stress from the substrate and the BTO film, and introduce tensile stress on the adjoining BTO layer.

In our study, and considering the above-mentioned epitaxial relationship, the out-of-plane lattice constant (denoted as the lattice parameter c) for each layer was determined by fitting the peaks corresponding to specific crystal planes of each layer in the measured specular θ-2θ curve (see Fig. 2a). We reported the measured c_{BTO} values as a function of θ_{BTO} in Fig. 2b. For a θ_{BTO} = 3 nm, both θ_{NFO} = 4 nm and 12 nm stacks exhibit a large c_{BTO} (4.192 Å and 4.201 Å, respectively), implying an out-of-plane stretching of the film. From an elasticity standpoint, this suggests significant in-plane compression of the BTO lattice. As θ_{BTO} grows from 3 nm to 12 nm, the strain imposed by the STO substrate decreases, causing a reduction in the c_{BTO} — down to 4.12 Å and 4.10 Å for θ_{NFO} = 4 nm and 12 nm samples, respectively. Increasing θ_{NFO} from 4 nm to 12 nm leads to a general decrease in the c_{BTO}, aligning with the notion that thicker NFO layers exert greater tensile stress on BTO, offsetting the compressive strain from STO. Even at rather high θ_{NFO} and θ_{BTO} (θ_{NFO} = 12 nm, θ_{BTO} = 9 nm), the compressive strain from substrate still dominates in BTO layer, with a mean tetragonality of 1.053, demonstrated by the 113 reciprocal space mapping in Fig. S2.

Conversely, c_{NFO} expands with increasing θ_{BTO} (see Fig. 2c), which aligns with the expectation that thicker BTO layers exert progressively more compressive stress on NFO. Specifically, when θ_{BTO} increases, c_{NFO} increases from 8.336 Å to 8.448 Å for samples with θ_{NFO} = 4 nm, while for samples with θ_{NFO} = 12 nm, c_{NFO} rises from 8.329 Å to 8.435 Å.

Surprisingly, c_{NFO} at minimal θ_{BTO} matches the cubic lattice parameter of NFO, suggesting that NFO is not under compressive stress from the STO substrate in this case. Further exploration revealed the absence of Laue oscillations in the 00L curves for samples with θ_{BTO} = 3 nm, hinting at non-coherence between deposited ferrite layer and the BTO layer. Such non-coherence often results in lattice mismatch being accommodated by dislocation formation at the interface layers *i.e.* plastic deformations, thereby alleviating stress. This phenomenon could also explain the slightly counter-intuitive trend observed when θ_{BTO} increases from 3 to 6 nm in samples with θ_{NFO} = 4 nm.

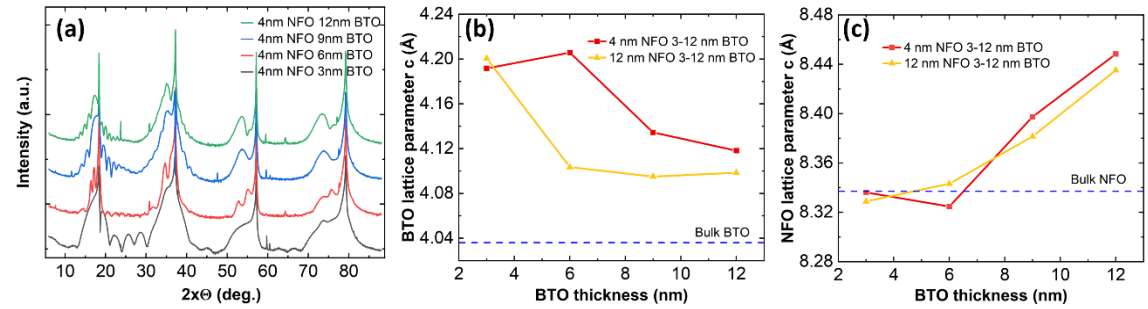

Figure 2. X-ray diffraction investigations of the layers. (a) 00L specular diffraction scans of four 4 nm thick NFO samples with 3, 6, 9 and 12 nm BTO respectively. (b) Out-of-plane lattice parameter of BTO in relation to BTO thickness for 4 nm and 12 nm thick NFO films. The lattice parameters were extracted *via* fitting of BTO (003) peaks in 00L diffraction patterns using Gaussian functions. (c) Out-of-plane lattice parameter of NFO as a function of BTO thickness for 4 nm and 12 nm thick NFO films.

Ferroelectric properties

The ferroelectric properties of the films were investigated using PFM. On each sample, nine square-in-square patterns of size 1 µm × 1 µm were written. The 9 patterns are written with static voltages ranging from 2 V to 7 V, as illustrated in Fig. S3. The internal square

was written with negative static voltage, while the external frame was written with positive static voltage. The voltage was applied to the PFM tip (located on the sample surface), while the substrate was grounded to the PFM chunk. After writing the pattern, to determine the layer's polarization, a 1 V AC drive voltage was applied to the sample at contact resonance frequency causing the films to expand and contract, with the response signal amplified using lock-in amplifier. Moreover, an additional DC offset voltage was applied and tuned to compensate for static charge effect[30]. To validate the reproducibility of our results, multiple square-in-square patterns were inscribed on various parts of the samples, with the results representing the predominant behavior observed across tests. Clear ferroelectric domain wall can be seen as the dark line situated between the inner square and outer frame in the amplitude images (first row of Fig. 3), and the phase contrast between these two parts (second row of Fig. 3). Typical line profiles across the written square-in-square pattern are shown in Fig. S4, providing quantitative evidence of the near-zero amplitude at the ferroelectric domain walls and the 180° phase difference between oppositely oriented ferroelectric domains.

First observation from the PFM read images is that the film's initial polarization was oriented upwards (pointing towards NFO layer), as evidenced by the alignment of polarization with the negatively polarized regions. Furthermore, when the PFM writing voltage lies above a certain threshold, the PFM-written square-in-square patterns emerge in the PFM read images, demonstrating a dual reversed out-of-plane polarization zone. Comparative analysis of the PFM read images for varying θ_{BTO} with θ_{NFO} = 4 nm unveiled that as θ_{BTO} decreases, lower PFM voltages are required to switch the out-of-plane polarization, especially from the initial up state to the down state. This reduction in reversal

voltage with respect to the downscaling of film thickness is a favorable characteristic for enhanced energy efficiency when considering device miniaturization. We will further investigate the origin behind this trend in the discussion section.

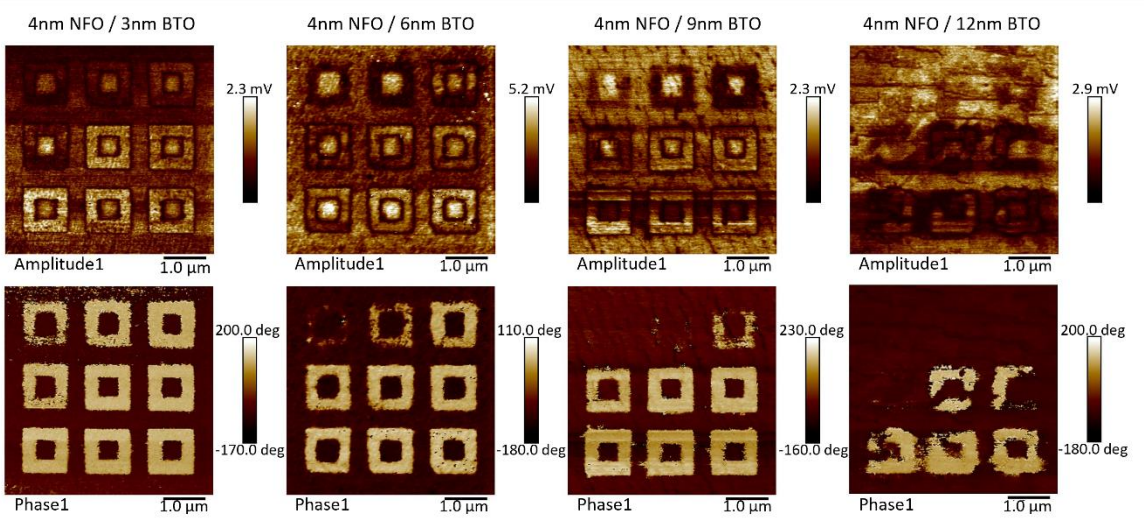

Figure 3. PFM signal *versus* θ_{BTO} for 4 nm NFO film samples. PFM amplitude images (top row) and phase images (bottom row) recorded on four 4nm-NFO samples with 3, 6, 9 and 12 nm thickness of BTO, after writing of 9 square-in-square patterns with PFM tip voltages at 2, 3, 4, 4.5, 5, 5.5, 6, 6.5, 7V respectively. The writing voltage increases from left to right and from top to bottom. The inner square is written in negative voltages.

Increasing θ_{NFO} from 4 nm to 12 nm led to a substantial deterioration of the PFM signal-to-noise ratio, as illustrated in Fig. 4. To elucidate the underlying cause of this phenomenon, it is imperative to establish an electrical circuit model of the deposited oxide heterostructures. While an ideal oxide layer is typically treated as a capacitor, an actual deposited oxide layer is often considered as a capacitor with a resistor in parallel, which accounts for any current leakage through imperfections in the layer[31–33]. Consequently, the

total impedance Z_{total} of the NFO and BTO oxide layers deposited on top of a conductive Nb:STO substrate, is expressed mathematically in Eq.(1):

$$Z_{\text{total}} = R_s + \frac{1}{j\omega C_{\text{BTO}} + \frac{1}{R_{\text{BTO}}}} + \frac{1}{j\omega C_{\text{NFO}} + \frac{1}{R_{\text{NFO}}}} \quad (1)$$

In this formula, R_s represents the resistance of the substrate and the test system, C_{BTO} and C_{NFO} denote the capacitances of the BTO and NFO layers, respectively, while R_{BTO} and R_{NFO} represent their leakage resistances.

PFM effectively detects the polarization by measuring the physical deformation of these layers in response to an applied AC drive voltage. The effective voltage experienced by the BTO layer can be calculated using impedance values, and is shown in Eq. (2):

$$V_{\text{BTO}} = \frac{V_{\text{total}} Z_{\text{BTO}}}{Z_{\text{total}}} = \frac{V_{\text{total}}}{1 + \left(j\omega C_{\text{BTO}} + \frac{1}{R_{\text{BTO}}}\right) R_s + \frac{j\omega C_{\text{BTO}} R_{\text{BTO}} R_{\text{NFO}} + R_{\text{NFO}}}{j\omega C_{\text{NFO}} R_{\text{BTO}} R_{\text{NFO}} + R_{\text{BTO}}}} \quad (2)$$

Considering that the capacitance of a parallel plate capacitor can be calculated using $C = \epsilon S/\theta$, where ϵ, S and θ are the dielectric constant, surface area, and thickness of the dielectric, respectively, it follows that as θ_{NFO} increases, C_{NFO} decreases, diverting a more significant portion of the 1 V AC drive voltage and reducing the V_{BTO}. Since PFM already defines sub-Å level lattice expansion by amplifying the signal, a reduced effective drive voltage on the BTO layer means a weaker response signal, hence a lower signal-to-noise ratio. Despite the lower signal-to-noise ratio, the general trend previously shown with θ_{NFO} = 4 nm samples (Fig. 3), which suggested that thinner BTO layers require a lower voltage to reverse their electric polarization, appears consistent with θ_{NFO} = 12 nm samples, when comparing the thinnest and thickest θ_{BTO} layers.

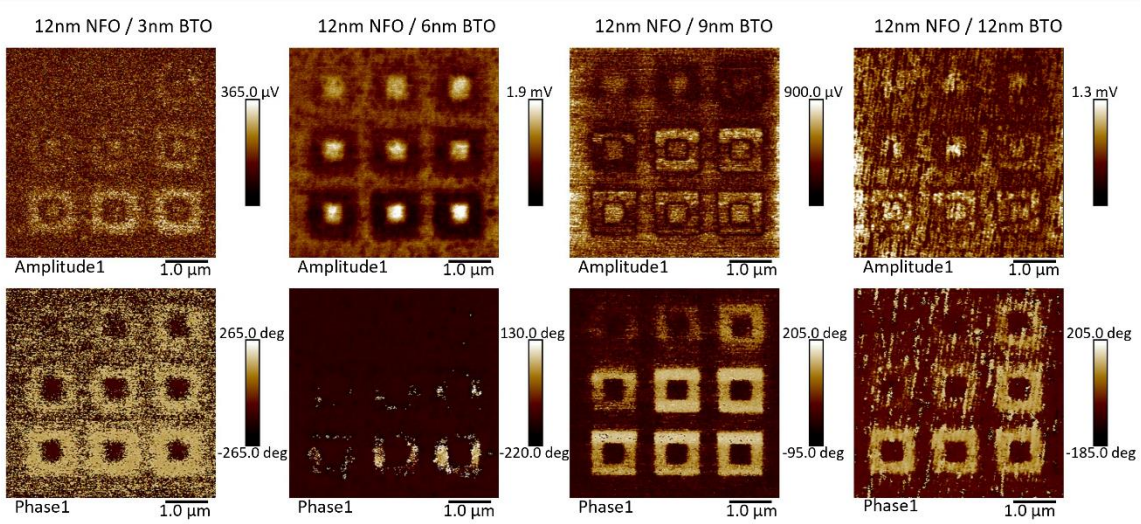

Figure 4. PFM signal *versus* θ_{BTO} for 12 nm NFO film samples. PFM amplitude images (top row) and phase images (bottom row) recorded on four 12 nm-NFO samples with 3, 6, 9 and 12 nm thickness of BTO, after writing of 9 square-in-square patterns with PFM tip voltages at 2, 3, 4, 4.5, 5, 5.5, 6, 6.5, 7V. The inner square is written in negative voltages.

Magnetic properties

After describing the ferroelectric properties in BTO, we will now analyze the variations of the NFO magnetic properties in our heterostructure samples with varying thickness.

The general formula for spinel structure is AB_2O_4, where A and B are different metal cations. In a normal-spinel structure, the A cations occupy the tetrahedral (T_d) sites, and the B cations occupy the octahedral (O_h) sites. Bulk NFO ideally adopts an inverse spinel structure[34,35], which means that Ni^{2+} cations (A cations) reside in O_h sites, while Fe^{3+} cations (B cations) are distributed equally between O_h and T_d sites. When NFO is in the form of thin films, it may exhibit a mixed spinel structure[36], intermediate between normal and inverse spinels, as also found in other spinel oxide systems[37,38]. These intermediate cation distributions can be quantified by the inversion parameter *y*, such as

$[Ni_{1-y}Fe_y]_{Td}[Ni_yFe_{2-y}]_{Oh}O_4$. In spinel oxides, y can vary from 0 (the completely normal spinel structure) to 1 (the completely inverse spinel structure). This parameter essentially tells us how the Ni^{2+} and Fe^{3+} ions are distributed between the T_d and O_h sites.

Regarding the magnetic ordering, NFO is ferrimagnetic because of the strong antiferromagnetic coupling between the magnetic moments of cations in O_h and T_d sites, every cation in a O_h or T_d sublattice being ferromagnetically coupled together. Given the spin magnetic moments of isolated Ni^{2+} (2 μ_B) and Fe^{3+} (5 μ_B) ions, this magnetic ordering would lead to a theoretical overall spin magnetic moment of 2 μ_B per NFO f. u., if the bulk NFO oxide adopts a perfectly inverse spinel structure ($y = 1$). Specifically, the theoretical spin magnetic moment contribution from all constituent Fe^{3+} ions is 0 μ_B, while that of Ni^{2+} is 2 μ_B. If NFO possesses a mixed spinel structure ($y < 1$), the total spin magnetic moment is expected to rise with decreasing y, with the formula $(-6y + 8)$ μ_B, ultimately reaching a value of 8 μ_B for $y = 0$, as previously confirmed by DFT calculations[25].

The focus here is on unraveling the magnetic characteristics of NFO layers and exploring how these characteristics relate to the broader context of multiferroic systems. This involves understanding the interaction between magnetic properties and other ferroic phenomena or the chemical environment within these systems. We employed XAS and XMCD techniques to delve into the magnetic properties and site distribution of ions within the NFO layers. XAS and XMCD are element specific and are fulfilled by tuning the X-ray energy to specific absorption edges of desired elements. For these samples, we probed the spectra at the Fe $L_{3,2}$ and Ni $L_{3,2}$ edges, utilizing an 1 T maximum magnetic field – determined sufficient by the saturation observed in the magnetic hysteresis loops (Fig. S5).

The analysis started with examining the spectra at the Fe $L_{3,2}$ edges. To interpret these spectra, we conducted ligand field multiplet calculations using the CTM4XAS[39] code, where we considered several factors including *3d* electron configurations of the cation, crystal field, spin-orbit coupling and electron-electron interaction[40,41]. This analysis helped us simulate the XAS and XMCD spectra for Fe ions in different sites: Fe^{3+} ions in octahedral sites (Fe^{3+}_{Oh}), Fe^{3+} ions in tetrahedral sites (Fe^{3+}_{Td}) and Fe^{2+} ions in octahedral sites (Fe^{2+}_{Oh}), as illustrated in Fig. 5a and 5b. All experimental XAS and XMCD spectra can be well reproduced by fitting them using linear combination of the calculated spectra, as shown in Fig. 5c and 5d. The distribution of Fe ions in each type of site is thus obtained from the corresponding proportion of XAS or XMCD spectra.

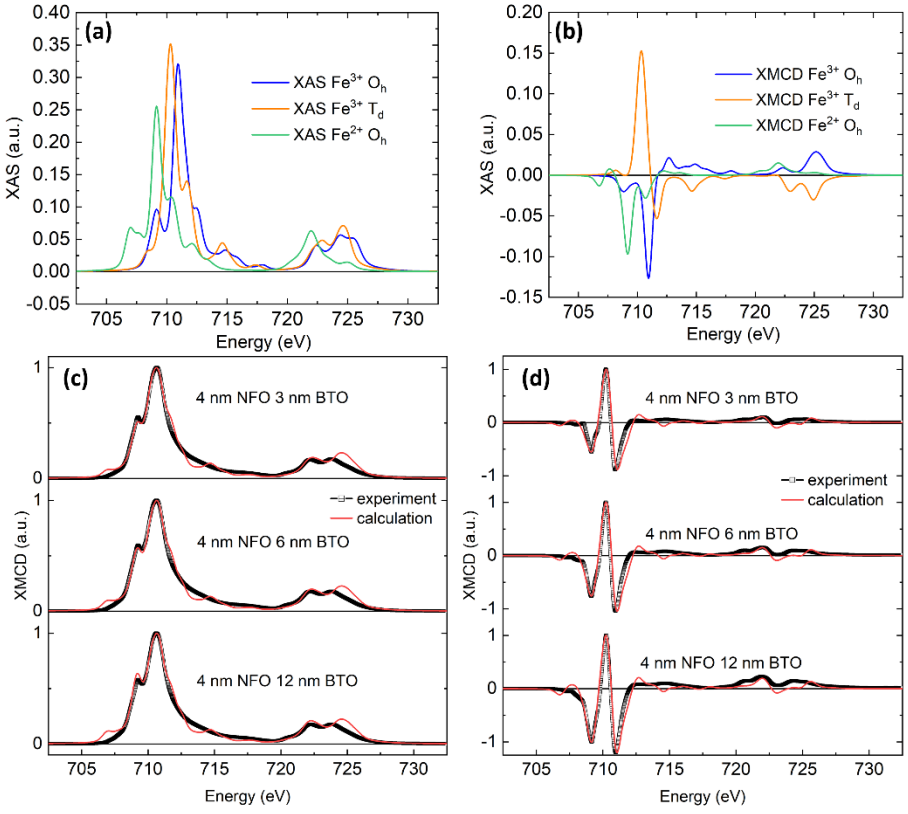

Figure 5. Calculated and experimental XAS and XMCD spectra at Fe $L_{3,2}$ edge. Calculated XAS (a) and XMCD (b) spectra at the $L_{3,2}$ edge for Fe^{3+}_{Oh}, Fe^{3+}_{Td} and Fe^{2+}_{Oh} sites.

Experimental XAS (c) and XMCD (d) spectra at the Fe $L_{3,2}$ edge for three 4 nm - NFO samples with 3, 6 and 12 nm of BTO fitted by using a linear combination of the calculated spectra in (a) and (b).

An intriguing trend emerged when considering how this distribution changes with θ_{BTO}, as demonstrated in Fig. 6a. Specifically, as θ_{BTO} increases, the Fe^{2+} proportion increases, and the Fe^{3+} proportion decreases. This reduction of Fe ions signifies a growing number of oxygen vacancies in the NFO layer with increasing θ_{BTO}. We will further discuss the possible mechanism of this phenomenon later in this paper by combining first-principles calculations. The inversion parameter y, ($y = 2 \times percentage\ of\ Fe^{3+}_{Td}$, see point 6 in supplementary materials), shows a decreasing trend from 0.81 to 0.65 as θ_{BTO} increases from 4 nm to 12 nm, which is thus expected to lead to an increase of the total spin magnetic moment.

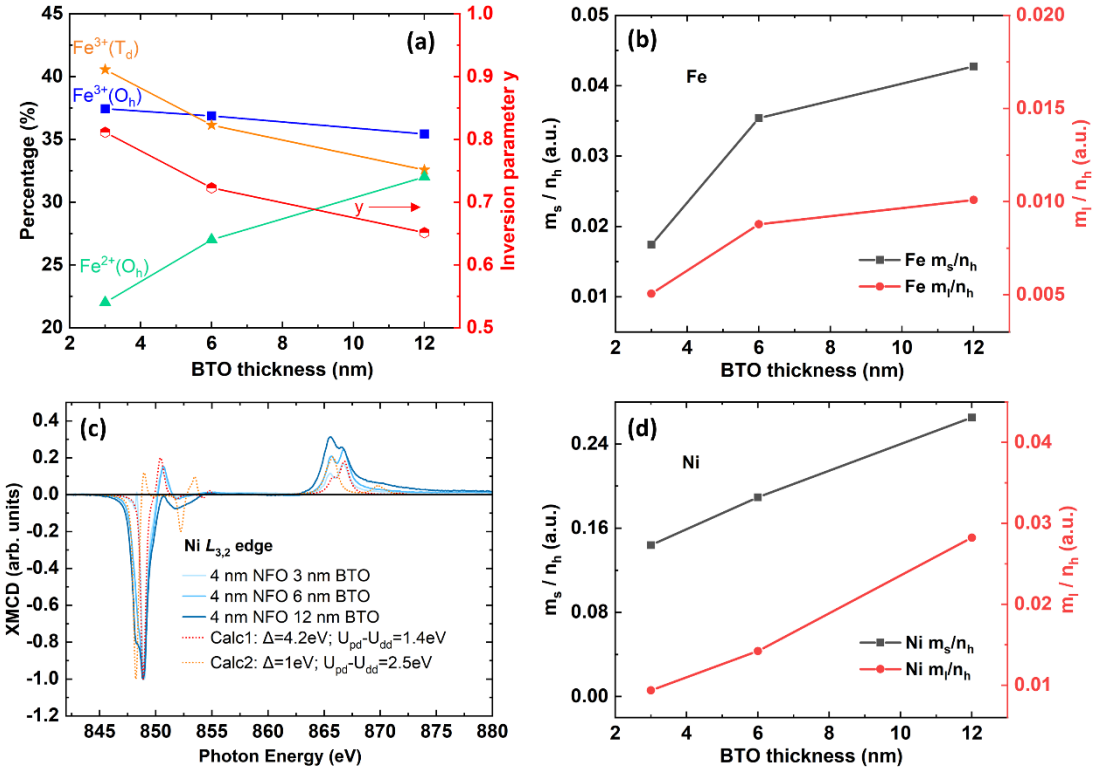

Figure 6. Variation of site distribution and magnetic moment for Fe and Ni ions as a function of θ_{BTO} for θ_{NFO} = 4 nm. (a) BTO thickness dependences of relative distribution of Fe_{Oh}^{3+}, Fe_{Td}^{3+} and Fe_{Oh}^{2+} ions, with corresponding inversion parameter *y* plotted and shown on the right axis. (b) Relative evolution of magnetic moments of the Fe ion calculated using sum rules as a function of BTO thickness. (c) Normalized experimental XMCD curves near Ni $L_{3,2}$ edge for three 4 nm - NFO samples with 3, 6 and 12 nm of BTO, as well as two calculated Ni_{Oh}^{2+} spectra (Calc1 and Calc2) each with their own sets of charge transfer parameters in multiplet model. (d) Relative evolution of magnetic moments of the Ni ion calculated using sum rules as a function of BTO thickness.

To get a better understanding on the evolution of the magnetic properties of the NFO layer in the NFO/BTO heterostructure, we applied sum rules[42,43] to XAS and XMCD spectra of each ion sites. This approach allowed us to extract spin and orbital magnetic moments of ions located in different sites within the NFO structure. Spin moment, instead of effective spin moment, can be extracted using spin sum rule here based on the two verified conditions[44]: firstly, L_2 and L_3 edges in the spectra are well separated and secondly the spin-quadrupole coupling is nearly zero in our system. The spin (m_s) and orbital magnetic moment (m_l) for each Fe ion site are calculated using Eq. (3) and (4)[43]:

$$\frac{m_s}{n_h} = -\frac{3p - 2q}{r} \tag{3}$$

$$\frac{m_l}{n_h} = -\frac{2q}{3r} \tag{4}$$

In these equations, n_h denotes the total number of valence holes in the electronic ground state, p is the integral of the XMCD signal of the L_3 edge region, q is the integral of the XMCD spectra of both L_3 and L_2 edge regions, and r is the integral of the isotropic XAS

spectrum over L_3 and L_2 edge region with subtraction of a step background produced by transitions to unoccupied continuum states. We use the decomposition of the spectra in three components (XAS/XMCD of Fe_{Oh}^{3+}, XAS/XMCD of Fe_{Td}^{3+}, XAS/XMCD of Fe_{Oh}^{2+}) in order to calculate spin and orbital moments for each site. The total spin and orbital moments of Fe ions are then calculated by summing over the spin and orbital moments of each available Fe sites weighted by the corresponding proportion of sites derived from the multiplet fitting. The evolution of total spin and orbital moments of Fe ions with θ_{BTO} is shown on Fig. 6b, where both the spin and orbital magnetic moments per valence hole demonstrate a trend of increase with increasing θ_{BTO}. This observation aligns well with our preliminary estimation derived from the relation between isolated spin magnetic moment and inversion parameter, that is, a higher inversion parameter induces smaller spin magnetic moment of Fe. Interestingly, the detailed analysis of magnetic moments associated with different types of Fe ions highlighted that Fe_{Oh}^{2+} uniquely demonstrated a significant increase in magnetic moment with increasing θ_{BTO}, as shown in Fig. S6. This observation is consistent with the increasing proportion of Fe_{Oh}^{2+} sites as the BTO layer thickens.

To achieve a comprehensive understanding of the magnetic properties of NFO, we extended our investigation to include the site distribution and magnetic moments of nickel (Ni) ions within the thin films. Interestingly, the experimental spectra for Ni ions across all measured thicknesses of NFO thin films closely matched the calculated spectra for Ni^{2+} ions in O_h sites, as shown in Fig. S7. This match suggests a minimal presence of Ni ions in other configurations, such as Ni^{2+} in T_d sites, or Ni ions in higher oxidation states (Ni_{Oh}^{3+}, Ni_{Td}^{3+}), similar to findings of Yosuke, *et al.*, [45]. Despite the resemblance of experimental

XAS and XMCD spectra only to the calculated spectra of Ni_{Oh}^{2+} site, the spectra undergo shape variations as θ_{BTO} changes. Moreover, the spin and orbital magnetic moment calculated via sum rules demonstrate an improved magnetism of Ni, as shown in Fig. 6d.

To understand the origin of these spectral shape changes and the enhancement in Ni's magnetism, we fine-tuned the parameters of Ni_{Oh}^{2+} site in the charge transfer multiplet model. Specifically, we considered 2 types of Ni_{Oh}^{2+} sites with different charge transfer energy Δ, and dissimilar difference between the core-hole coulomb energy U_{pd} and on-site Coulomb energy U_{dd} (*i.e.* $U_{pd} - U_{dd}$). For the first type (Calculated 1 in Fig. 6c), parameters come from literature[45,46], and for the second type (Calculated 2 in Fig. 6c), an alternate set of parameters, which are explained below, are used and correspond to a lower value for Δ and higher value for $U_{pd} - U_{dd}$. The fit within this model is represented in Fig. 7 for two different films. One observes that as the θ_{BTO} increases from 4 to 12 nm, the percentage of the Calc2 (Calculated 2) increases from 20% to 47%.

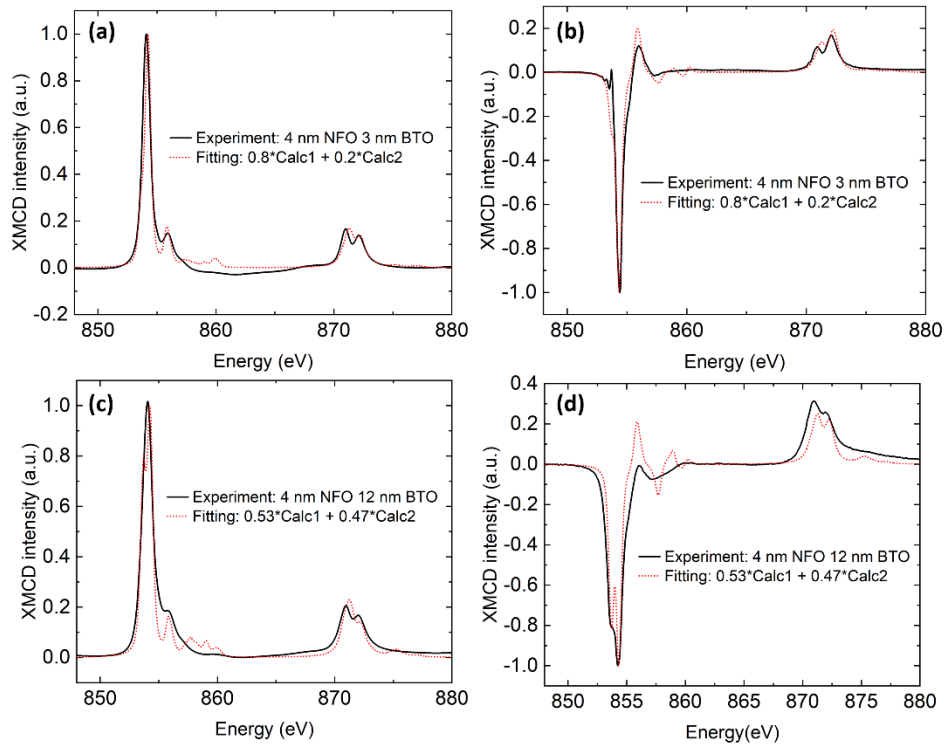

Figure 7. Experimental XAS and XMCD spectra at the Ni $L_{3,2}$ edge and corresponding multiplet fitting. Experimental XAS (a) and XMCD (b) spectra at the Ni $L_{3,2}$ edge for the 4 nm NFO/3 nm BTO sample, fitted by the linear combination of two calculated Ni_{Oh}^{2+} spectra with distinct sets of charge transfer parameters in multiplet model (shown in Fig. 6c – Calculated 1 and Calculated 2, see text). Similarly, panels (c) and (d) represent respectively the experimental XAS and XMCD spectra, with their corresponding multiplet fitting for the 4 nm NFO/12 nm BTO sample.

The charge transfer energy (Δ), in this context refers to the charge transfer energy in the initial state (before X-ray photon absorption), written as $\Delta = \Delta_i = E\left(d^{n+1}\underline{L}\right) - E(d^n)$, where $\underline{L}$ denotes a hole in the ligand (i.e. O 2p orbitals here), and $E\left(d^{n+1}\underline{L}\right)$ and $E(d^n)$ denote the multiplet averaged energies of the charge transfer and ionic configurations, respectively. Conversely, the charge transfer energy in the final state $\Delta_f = E\left(\underline{c}d^{n+1}\underline{L}\right) -$

$E(\underline{c}d^{n})$, where $\underline{c}$ denotes the core hole of Ni ion here, is estimated as $\Delta_f = \Delta_i - (U_{pd} - U_{dd}) = \Delta - (U_{pd} - U_{dd})$.[47] Hence, the decreased Δ and increased $U_{pd} - U_{dd}$ in Calc2 of Ni_{Oh}^{2+} spectrum signifies a smaller charge transfer energy in initial state Δ_i and in final state Δ_f in comparison with Calc1. A smaller Δ_i and Δ_f in Calc2 than in Calc1 means an easier transfer of electron between metal orbital and ligand orbital[48] in Calc2, implying a higher degree of overlapping between Ni *d*-orbitals and ligand *p*-orbitals in the sample plane, which can be introduced by the increased compressive in-plane strain imposed on NFO layer. This corresponds well with the discovery that increased proportion of Calc2 is needed to fit the experimental spectrum, with increasing θ_{BTO}, which has been proved to impose higher in-plane compressive strain on NFO layer in the structural properties section. Due to the complex interplay of various factors, including exchange interactions and lattice symmetry among others, the increased in-plane orbital overlap does not straightforwardly explain the observed increase in out-of-plane magnetic moments of Ni. This aspect will be further explored in the discussion section.

Considering the variation of Ni and Fe site distribution together, we observe an interesting phenomenon: the decrease in the proportion of Fe_{Td}^{3+} does not coincide with the appearance of Ni_{Td}^{2+}, since the fit of Ni spectra can be done with only Ni_{Oh}^{2+} of Calc1 or Calc2 type. That is in discrepancy with the conventional understanding of the transition between inverse and direct spinel structure. Here, without Ni^{2+} filling the vacated Td sites, the leaving Fe^{3+} from T_d sites leads to the formation of T_d vacancies in the NFO thin films. We quantified the relationship between the proportion of T_d vacancies and θ_{BTO}, revealing a clear trend presented in Fig. S11(b), with a detailed formula derivation provided in the

supplementary material (point 7). The implications of T_d vacancies will be further presented in the discussion section.

Additionally, considering that the oxidation degree of Ni cations is +2 ($n_h = 2$) and using the measured spin magnetic moment per valence holes (m_s/n_h) shown in Fig. 6d, the spin magnetic moments (m_s) of Ni in the 4 nm NFO/BTO heterostructures of varying thicknesses (4 nm NFO with 3, 6, 9, and 12 nm BTO) range between 0.3-0.5 μ_B, significantly smaller than the nominal value of the spin magnetic moment of isolated Ni^{2+} (2 μ_B). This kind of reduced magnetism has been identified by many studies in spinel thin films[45,49–53], where annealing has been proposed as possible remedy by some[45,53].

To understand the origin of the reduced magnetism and find the mechanism behind the remedial effect of annealing, we examined the effects of both air annealing and vacuum annealing on the NFO/BTO heterostructures. To study the air annealing effect, two additional samples, representative of the two observed behaviors, were prepared and investigated. More specifically, a 4 nm NFO/4.5 nm BTO sample, fabricated under analogous growth conditions, was cut into 2 parts: one portion air annealed at 450 °C for 3 hours, and the other left intact. Similarly, a 7 nm NFO/9 nm BTO sample was made and treated identically. The impact of air annealing is notably different for these two sets of samples, with a pronounced improvement in the XMCD intensity for Fe and Ni in the thinner NFO/BTO combination, as shown in Fig. S8. Furthermore, the magnetic hysteresis loops of these two sets of samples demonstrate the saturation of magnetization during absorption measurement, as illustrated in Fig. S9. Qualitatively, this improvement in XMCD intensity signifies an enhancement of the Fe and Ni magnetic moments after air annealing. Quantitative information about site distribution and magnetic moments are

deduced from multiplet fitting and sum rules (after decomposition of spectra in three components like before) (Fig. S10 and Fig. 8). For the thinner layer combinations, air annealing results in an obvious oxidation of the NFO layer (Fig. $8a_1$), substantial increases in the overall magnetic moments for both Fe (Fig. $8a_2$) and Ni ions (Fig. $8a_3$), and increases in absolute value of spin magnetic moments across all Fe ion sites (Fig. $S10a_1$). Contrastingly, the thicker NFO/BTO sample exhibits only marginal changes post-annealing, including a slight oxidation (Fig. $8b_1$), a modest improvement of Ni magnetic moments (Fig. $8b_3$), and a small decrease in the Fe magnetic moment (Fig. $8b_2$). This contrast underscores the much more significant effect of air annealing on improving the XMCD-deduced magnetic moments in thin NFO films. Given the depth sensitivity of the Total Electron Yield (TEY) mode used for X-ray absorption detection, the magnetic properties revealed by XMCD predominantly reflect the surface or near-surface regions of the samples, approximately 2 - 5 nm deep[54]. As a result, in the 4 nm NFO/4.5 nm BTO sample, the magnetic moments revealed by XMCD provides information on the whole film including the NFO/BTO interface. Otherwise, little information about interface in the 7 nm NFO/9 nm BTO sample can be extracted from XMCD. These findings suggest that in the very thin film, the presence of a substantial magnetically "dead" layer at the NFO/BTO interface that can potentially be revitalized through air annealing, the rest of the sample being insensitive to air annealing. The XMCD observation is hardly of any help to conclude upon the presence or not of this buried “dead” layer within the thick sample.

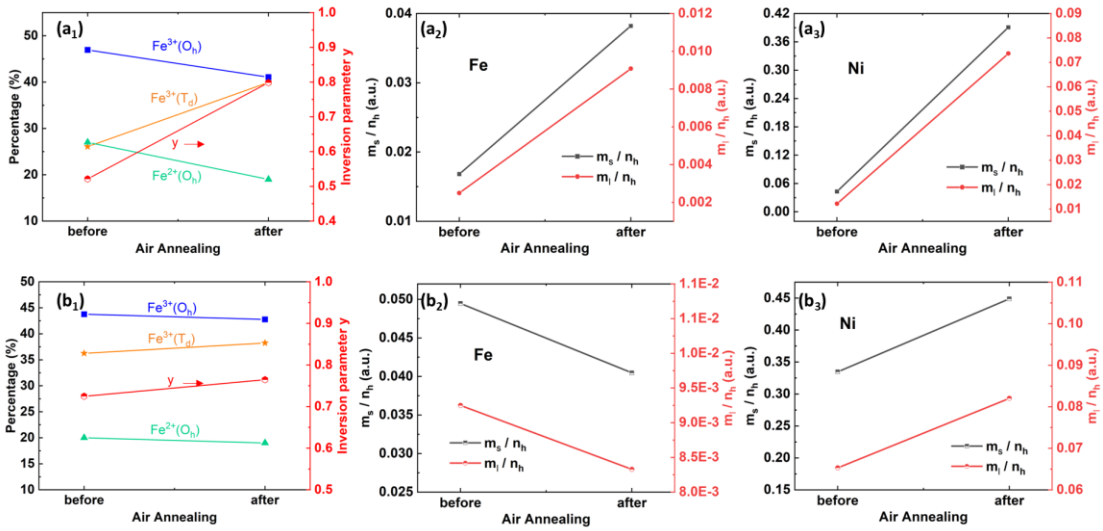

Figure 8. Air annealing effect on site distribution and magnetic moments of Fe and Ni ions. Air annealing influence on relative distribution of Fe^{3+}_{Oh}, Fe^{3+}_{Td} and Fe^{2+}_{Oh} ions, with corresponding inversion parameter y for (a_1) 4 nm NFO/4.5 nm BTO sample and (b_1) 7 nm NFO/9 nm BTO sample. Evolution of magnetic moments of the Fe ion calculated using sum rules with respect to air annealing for (a_2) 4 nm NFO/4.5 nm BTO, and (b_2) 7 nm NFO/9 nm BTO sample. The evolution of Ni magnetic moments for (a_3) 4 nm NFO/4.5 nm BTO, and (b_3) 7 nm NFO/9 nm BTO sample.

To further understand the mechanisms by which air annealing remedies the reduced magnetism, we extended our analysis to include vacuum annealing, conducted at 450 °C for 3 hours (the same as air annealing). Fig. 9 presents the results due to vacuum annealing of the three 4 nm – NFO samples with 3, 6, 12 nm of BTO studied in the first part of the paper. Fig. 9a illustrates that vacuum annealing induces a reduction of Fe^{3+} toward Fe^{2+}_{Oh} for most of the thickness combinations. Interestingly, the spin magnetic moment of Fe ions does not manifest noticeable changes, whereas the orbital magnetic moment only undergoes a slight increase with vacuum annealing, as depicted in Fig. 9b. Conversely, the

spin magnetic moment of Ni displays a decrease of around 10%, while its orbital magnetic moment doubled, as shown in Fig. 9c. This observation suggests that vacuum annealing does not effectively counteract the issues associated with the magnetically dead layer within these samples with very low NFO thickness. Indeed, if the vacuum annealing could cure the magnetically dead layer as air annealing, one would observe a significant improvement of the magnetic moment of Ni and each site of Fe, which is not observed (Fig. 9c and Fig. S6). Moreover, considering the samples' limited thickness (4 nm of NFO), which implies that XMCD analysis should reveal interface magnetic properties, the absence of magnetic moment enhancement further underscores the ineffectiveness of vacuum annealing in this context. Therefore, we infer that vacuum annealing does not adequately remedy the magnetically dead layer issue and might even exacerbate it, stressing that the presence of oxygen during the annealing process is crucial. The synergistic effect of heat and oxygen emerges as the key to addressing the magnetically dead layer challenge.

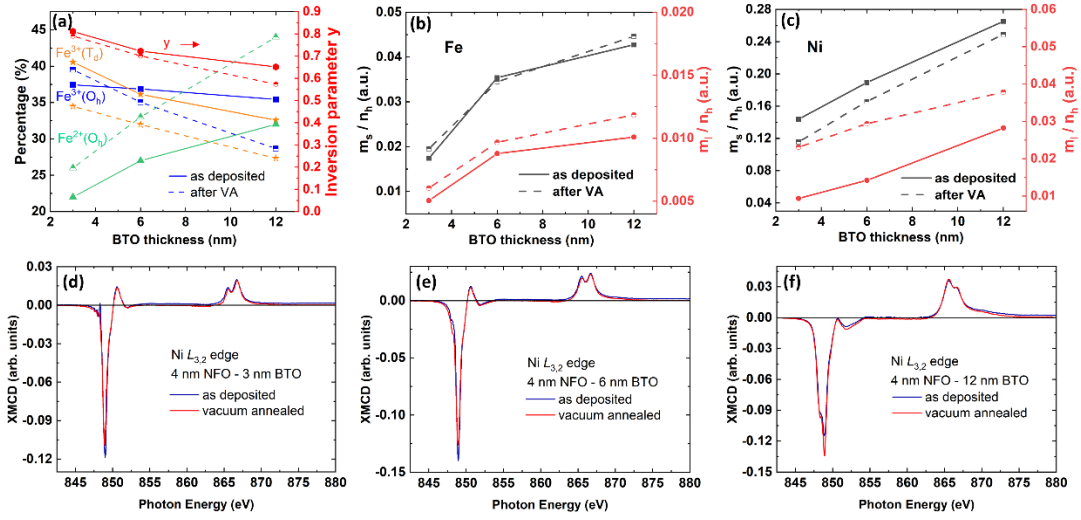

Figure 9. Vacuum annealing effects *versus* θ_{BTO} for 4 nm NFO samples. (a) Relative distribution of Fe_{Oh}^{3+}, Fe_{Td}^{3+} and Fe_{Oh}^{2+} ions, as well as inversion parameter y for as-deposited

(solid line) and vacuum-annealed (dash line) samples. Magnetic moments of (b) Fe ions and of (c) Ni ions, calculated using sum rules for as-deposited (solid line) and vacuum-annealed (dash line) samples. (d-f) Normalized experimental XMCD spectra for as-deposited samples (blue line) and vacuum annealed samples (red line) with increasing θ_{BTO} (from left to right).

First-principles calculations of the strain effect

We performed *ab initio* calculations in order to simulate the NFO electronic structure as a function of strain. In our investigation, we applied a compressive and biaxial in-plane strain to bulk NFO, spanning from 0% to -6%. For each strain state, we optimized the equilibrium out-of-plane lattice parameter and the positions of every atom by minimizing the forces and the out-of-plane stress. The results are summarized in Table 1. The first effect of the compressive strain is to induce a linear decrease of the fundamental band gap, which is reduced from 1.34 eV to 0.98 eV, *i.e.* by 27%, when the strain varies from 0% to -6%, while the c/a ratio increases linearly from 1.002 to 1.135. With the same variation of strain, we calculated that the formation energy of neutral oxygen vacancies decreases by 0.338 eV. Our calculations thus confirm that the variation of the strain state can contribute to facilitating the formation of oxygen vacancies. In addition to the epitaxial strain, other structural parameters, such as surface or interface effects (out-of-plane strain, polar distortions, or charge discontinuities) could also be responsible of the promotion of oxygen vacancies. In a former study[55], we for example demonstrated that more oxygen vacancies are likely to be present when the inversion degree is decreased, this last one being also subjected to be influenced by the strain[35]. Conversely, the presence of oxygen vacancies

can increase the cation disorder, increase the cationic mobility[56] and potentially promote the formation of new oxide phases[57].

In the section detailing structural properties, we discussed how an increase in θ_{BTO} applies greater compressive strain to the NFO layer. Specifically, as θ_{BTO} increases from 4 nm to 12 nm, the strain in 4 nm NFO increases from -2% to -3.8%, where minus sign denotes compressive strain. This strain leads to a transformation in the NFO layer's lattice structure from cubic to tetragonal. Our first-principles calculations reveal that this enhanced compressive strain effectively lowers the formation energy of oxygen vacancies in the NFO layer. Such a reduction in formation energy of oxygen vacancies facilitates the transformation of iron (Fe) ions from the 3+ to the 2+ oxidation state within the NFO layer as the BTO thickness increases, consistent with the experimental results of XMCD multiplet fitting in the magnetic properties section. This correlation between the BTO-induced strain and the observed modification in the valence state of Fe ions underscores the direct influence of mechanical stress from the BTO layer on the chemical composition and electronic structure of the NFO layer, providing a clear mechanistic understanding of the strain-induced changes in the NFO layer.

Strain (%)	c/a	E_g *(eV)*	m_s (μ_B)				$\Delta E_f[V_O]$ (meV)
			Fe_{Td}	Fe_{Oh}	Ni_{Oh}	O	
0	1.002	1.34	−3.884	4.037	1.553	0.076	0.0
−2	1.046	1.22	−3.872	4.030	1.545	0.077	−29.7
−4	1.090	1.14	−3.861	4.021	1.537	0.078	−134.7
−6	1.135	0.98	−3.851	4.010	1.527	0.081	−338.5

Table 1. Ratio between the out-of-plane and in-plane lattice parameters c/a, band gap at the Fermi level E_g, averaged spin magnetic moment per atom m_s, and variation of the

oxygen-vacancy formation energy $\Delta E_f[V_O]$ calculated from first-principles calculations for bulk $NiFe_2O_4$ in its perfectly inverse structure.

About strain effect on magnetic properties, the calculated m_s of Ni in NFO marginally decreases by 0.5% as the strain increases from -2% to -4%. However, the experimental finding shows 84% increase in m_s of Ni as the strain increases from -2% to -3.8%. This discrepancy suggests that strain is not the only effect that influence the Ni magnetic moment in NFO layer as θ_{BTO} increases. We will explore this discrepancy with possible explanation in the discussion section.

4. Discussion

For ferroelectric properties in NFO/BTO heterostructures, the observed increase in threshold voltage with increasing θ_{BTO} can be elucidated by examining the factors influencing the stabilization of electric polarization. The stabilization of the electric polarization primarily relies on the effective screening of the depolarization field by the interface or surface separating the ferroelectric layer from adjacent layers or the ambient environment.[12,58,59] The efficiency of this screening process can be influenced by various parameters, including but not limited to, the conductivity of the screening layer, surface adatoms, surface adsorption, and interface defects. In our investigation, increasing θ_{BTO} was found to induce a reduction of the NFO layer by converting Fe^{3+} ions to Fe^{2+}. This process is facilitated by the generation of oxygen vacancies, which is a direct result of the increased compressive strain from the BTO layer, as corroborated by X-ray diffraction analyses and first-principles calculations. Prior research has established that nickel ferrites with higher oxygen vacancies exhibit enhanced conductivity.[34,60,61] Better conductivity leads to higher screening efficiency of the depolarization field of the BTO layer, making its electric polarization more stable, and thus causes an increase in the threshold voltage as observed by PFM and shown in Fig. 3.

Counterintuitively, this behavior is different from the observations reported in our previous study on $CoFe_2O_4$ (CFO)/BTO systems.[62] For CFO/BTO systems, oxidation-reduction can be achieved between Co and Fe ions without the necessity of creating oxygen vacancies. Indeed, the tetragonality induced by thickness variation dominates the stability of the electric polarization in CFO/BTO system. The disparity between the CFO/BTO and NFO/BTO systems underscores the profound influence that substituting the cation in the

ferrite spinel has on the polarization characteristics, revealing the complex interdependencies between material composition, structural properties, and ferroelectric behavior.

About the magnetic properties, we evidenced a magnetically dead layer at the NFO/BTO interface in very thin NFO film samples, which is highly detrimental for the realization of spintronics devices requiring very thin layers like spin-filters of tunnel junctions. This characteristic poses significant challenges to reducing the thickness of magnetic layers in device applications and has been a subject of extensive investigation across various spinel systems. Antiphase boundaries[63,64] and vacancies at T_d sites[45] have been proposed as potential explanation for the nature of the magnetically dead layer. Specifically, the presence of high proportion of T_d vacancies is believed to suppress the magnetization in NFO through decreasing the superexchange interaction which establish the ferrimagnetic ordering[45]. Although the study herein does not allow for a definitive conclusion on the role of antiphase boundaries, our experiments on annealing effects not only identified the magnetism restoration techniques, but also shed some light on the nature of magnetically dead layer in our system. Specifically, we discovered that air annealing, in contrast to vacuum annealing, effectively enhances the magnetic moments of Ni and Fe ions in the 4-nm-thick NFO sample, suggesting a remediation of the magnetically dead layer which is thus not intrinsically linked to the layer thickness. This improvement in magnetic moment correlates with a reduction in the T_d and oxygen vacancies (Fig. S11a), implicating these vacancies in the formation of the magnetically dead layer. However, this observation seemingly contradicts our findings related to the effect of BTO thickness on the NFO's magnetic properties, where an increase in BTO thickness leads to enhanced magnetic

moments for Fe and Ni, despite an apparent increase in T_d and oxygen vacancies. This discrepancy indicates that T_d and oxygen vacancies alone cannot fully account for the magnetically dead layer phenomenon.

To unveil the physical and chemical nature of this magnetically dead layer, we examined in detail the RHEED patterns during film growth especially for the thickness regime prior to the appearance of the spinel extra streaks, which can provide the type of crystal structure and the evolution of in-plane lattice parameters. The results revealed an intermediate cubic phase in the initial 2-3 nm of thin film growth, identified by the appearance of spinel streaks only after about 2.3 nm of growth and the presence of an intermediate plateau of the evolution of in-plane lattice parameter, as shown in Fig. 10. Based on the observed lattice parameter and cubic structure, we hypothesize the formation of antiferromagnetic rock salt phases of NiO and FeO at the onset of deposition. The antiferromagnetic nature of these phases are likely to explain the observed decrease in magnetization. Given the similarity of lattice parameter of NiO (4.177 Å)[65] and FeO (4.33 Å)[66] to that of BTO (3.992 Å)[27], the RHEED patterns of these phases closely resemble those of BTO with only small decreases in the spacing of the streaks, which explains why this phase remains elusive during the real-time RHEED monitoring of growth. The presence of Ni^{2+} and Fe^{2+} in octahedral sites within these rock salt structures, with similar symmetry with Ni_{Oh}^{2+} and Fe_{Oh}^{2+} in spinel NFO, making it difficult to distinguish using XAS and XMCD spectra.

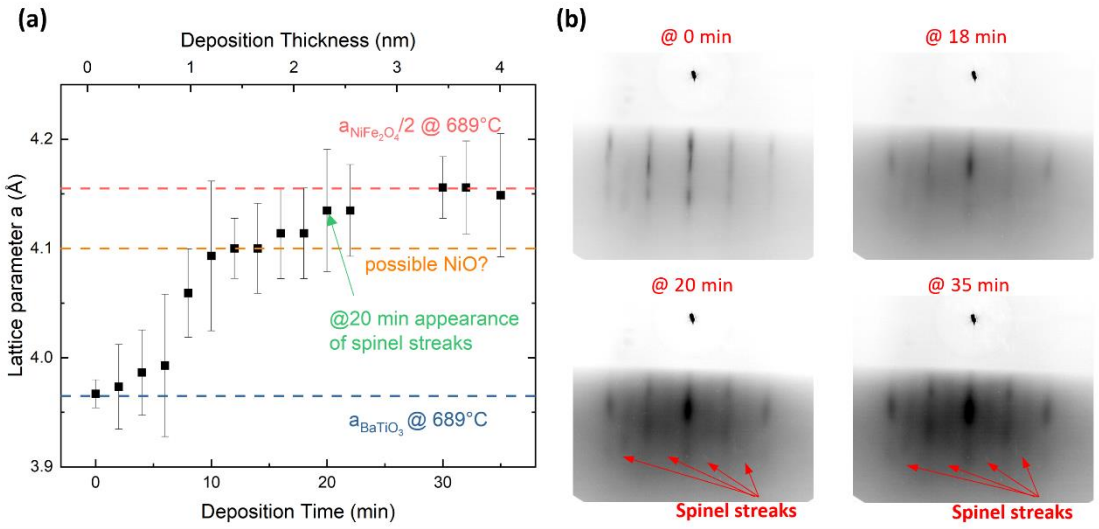

Figure 10. Crystal structure information obtained from RHEED images during deposition of 4 nm NFO on 4.5 nm BTO. (a) Evolution of in-plane lattice parameter during epitaxial growth of 4 nm NFO at 689 °C oven temperature (real temperature of sample is slightly smaller) calculated from RHEED streak spacing. Note an intermediate plateau during 10-18 mins of growth, suggesting an intermediate phase. (b) RHEED images taken at various deposition moments of the 4 nm NFO growth. Note that starting from 20 min, the number of streaks doubles, proving that crystal structure changes into spinel structure, with nearly two times the lattice parameter of former structure. It also signifies that the first 2-3 nm layer grown between 0-18 min is not of spinel structure.

If our hypothesis holds, it provides a mechanistic understanding of how oxygen and heat synergistically facilitate magnetism restoration through a redox reaction: $NiO + FeO + O_2 \xrightarrow{\Delta} NiFe_2O_4$, necessitating heat ($\Delta$) for ion mobilization and oxygen for Fe ion oxidation. The proposed transformation from rock salt to spinel structure - and their coexistence - aligns with findings from prior studies[67–69]. Since the FeO is bulk metastable, as the layer thickness increases above certain threshold, this intermediate NiO/FeO layer may also

vanish and transform into NFO, analogous to transformation of intermediate $\gamma - Fe_2O_3$ to $\alpha - Fe_2O_3$ in our previous work[70]. This self-transformation may explain the absence of this intermediate phase in HRTEM image in thicker NFO sample. Moreover, this theory also explains the calculated high proportion of T_d vacancies. We calculated the T_d vacancies based on the assumption that all Ni and Fe ions reside in spinel structures, which provides both O_h and T_d sites. Yet, this assumption is in fact not applicable because the first several nanometers of growth form an intermediate NiO/FeO layer with rock salt structure, providing only O_h sites. This is why a large proportion of T_d vacancies was obtained, in short, we consider a number of in fact non-existing T_d sites. Furthermore, it is intuitive to suppose that the thickness and/or properties of this intermediate NiO/FeO layer may vary as the thickness of BTO changes. Without considering this intermediate NiO/FeO layer in our first-principles calculations, this may explain the discrepancy between the experimentally observed slightly improved magnetic moments with increasing θ_{BTO} and the nearly stable or marginally reduced trend in the first-principles calculations.

Future research could include comprehensive HRTEM investigations of ultra thin NFO film heterostructures to provide more direct and unambiguous evidence of the presence of this intermediate NiO/FeO interfacial layer.

5. Conclusions

In this investigation, we delved into the properties of a series of NFO/BTO multilayers by varying BTO and NFO thicknesses and post-deposition anneal treatment. Through comprehensive analysis as well as first-principles calculations, we unveil the strain, chemistry, ferroelectric, and magnetic properties as well as their interrelationships at NFO/BTO interfaces.

Our XRD experiments revealed that with an increase in BTO thickness, the BTO layer tends to relax from the compressive strain imposed by the substrate. Simultaneously, it imparts an augmented compressive force onto the interfacial NFO layer. By fitting XMCD spectra lines using multiplet theory, we observed chemical reduction of Fe ions originated from a surge in oxygen vacancies within NFO layer. We postulated that this increase in oxygen vacancies is predominantly due to the intensified compressive strain within the film, proved by the lower formation energy of oxygen vacancies calculated by first-principles calculations.

Moreover, PFM detection pinpointed enhanced stability of the electric polarization in systems with thicker BTO. This is attributed to oxygen vacancy enhanced conductivity in the NFO side of NFO/BTO interface. The bolstered conductivity strengthens the screening effect, thereby stabilizing the polarization.

Most importantly, the magnetic moments deduced from XMCD curves highlighted a potential magnetically dead layer suppressing magnetization in very thin NFO film heterostructures. Additionally, increasing thickness of BTO layer can slightly improve the magnetic moments, while increasing NFO thickness can well restore the magnetic moments. Subsequent XMCD tests for pre and post air/vacuum annealing samples, as well as detailed RHEED analysis on the crystal structure during growth, lead to a theory that the nature of magnetically dead layer in very thin film is around 2 nm of antiferromagnetic rock salt structure NiO and FeO formed before the formation of spinel NFO. Air annealing was proved to effectively optimize the magnetic moments at the interfaces. It was established that air annealing improves the magnetism by transforming the

antiferromagnetic NiO/FeO intermediate layer into spinel NFO *via* the redox reaction under the synergistic outcome of oxygen and temperature/heat.

Our results allow proposing a number of improvements enabling optimal multiferroic behavior in the NFO/BTO system, with a special focus on magnetic properties at the interface. Air annealing at moderate temperature is observed as being highly favorable for improving magnetic performance in the thin film regime opening the route for exploiting the high resistivity of NFO in very thin film spintronics applications.

ASSOCIATED CONTENT

Supporting Information

The Supporting Information is available at the end of this document.

PFM poling and reading experimental details, scanning modes, tips, heads, and height sensor images and data; relative deformation calculated data; electrical measurements setup and leakage currents; complementary RHEED patterns at the end of the growth.

Author Contributions

The manuscript was written by H.L with contributions of all authors. Sample preparation and treatment was carried out by A.B. and H.L. XRD measurement was performed by C.M, H.L. and A.B. PFM measurement was performed by H.L. under the guidance of C.LR. XAS and XMCD measurements were fulfilled by P.O., A.B., H.L., and C.B. First-principles calculations were conducted by R.A. All authors have given approval to the final version of the manuscript.

Notes

The authors declare no competing financial interest.

ACKNOWLEDGMENT

H.L. and A.B. thank Christophe Gatel, Cécile Marcelot, Robin Cours and Leifeng Zhang for FIB preparation and HRTEM samples at CEMES Toulouse.

Funding Sources: The authors acknowledge the “Agence Nationale de la Recherche (ANR)” for their funding through the MULTINANO project (Grant ANR19-CE09-0036)

and IOBTO project (Grant ANR-15-CE09-0005-01). We acknowledge the financial support from the CNRS-CEA “METSA” French network for the FIB and TEM experiments conducted on the CEMES platform. This work was also supported in part by “Triangle de la Physique,” “PHOM” and “Ile-de-France” (C’Nano IdF, DIM-OXYMORE, DIM-MAP, and ISC-PIF) under the IMAFMP and MAEBA grants. We acknowledge Synchrotron SOLEIL for provision of synchrotron radiation facilities and are grateful for assistance while using DEIMOS and DiffAbs beamlines. This work was granted access to the HPC resources of CALMIP (Allocation No. 2023-2024/P1229).

References

(1) Heron, J. T.; Bosse, J. L.; He, Q.; Gao, Y.; Trassin, M.; Ye, L.; Clarkson, J. D.; Wang, C.; Liu, J.; Salahuddin, S.; Ralph, D. C.; Schlom, D. G.; Íñiguez, J.; Huey, B. D.; Ramesh, R. Deterministic Switching of Ferromagnetism at Room Temperature Using an Electric Field. *Nature* **2014**, *516* (7531), 370–373. DOI: 10.1038/nature14004.

(2) Manipatruni, S.; Nikonov, D. E.; Lin, C.-C.; Gosavi, T. A.; Liu, H.; Prasad, B.; Huang, Y.-L.; Bonturim, E.; Ramesh, R.; Young, I. A. Scalable Energy-Efficient Magnetoelectric Spin–Orbit Logic. *Nature* **2019**, *565* (7737), 35–42. DOI: 10.1038/s41586-018-0770-2.

(3) Fiebig, M.; Lottermoser, T.; Meier, D.; Trassin, M. The Evolution of Multiferroics. *Nat. Rev. Mater.* **2016**, *1* (8), 16046. DOI: 10.1038/natrevmats.2016.46.

(4) Jia, T.; Cheng, Z.; Zhao, H.; Kimura, H. Domain Switching in Single-Phase Multiferroics. *Appl. Phys. Rev.* **2018**, *5* (2), 021102. DOI: 10.1063/1.5018872.

(5) Patel, S. K.; Robertson, D. D.; Cheema, S. S.; Salahuddin, S.; Tolbert, S. H. In-Situ Measurement of Magnetoelectric Coupling and Strain Transfer in Multiferroic Nanocomposites of $CoFe_2O_4$ and $Hf_{0.5}Zr_{0.5}O_2$ with Residual Porosity. *Nano Lett.* **2023**, *23* (8), 3267–3273. DOI: 10.1021/acs.nanolett.3c00083.

(6) Zheng, H.; Wang, J.; Lofland, S. E.; Ma, Z.; Mohaddes-Ardabili, L.; Zhao, T.; Salamanca-Riba, L.; Shinde, S. R.; Ogale, S. B.; Bai, F.; Viehland, D.; Jia, Y.; Schlom, D. G.; Wuttig, M.; Roytburd, A.; Ramesh, R. Multiferroic $BaTiO_3$-$CoFe_2O_4$ Nanostructures. *Science* **2004**, *303* (5658), 661–663. DOI: 10.1126/science.1094207.

(7) Sharma, Y.; Agarwal, R.; Collins, L.; Zheng, Q.; Ievlev, A. V.; Hermann, R. P.; Cooper, V. R.; Kc, S.; Ivanov, I. N.; Katiyar, R. S.; Kalinin, S. V.; Lee, H. N.; Hong, S.; Ward, T. Z. Self-Assembled Room Temperature Multiferroic $BiFeO_3$ -$LiFe_5O_8$ Nanocomposites. *Adv. Funct. Mater.* **2020**, *30* (3), 1906849. DOI: 10.1002/adfm.201906849.

(8) Mundy, J. A.; Brooks, C. M.; Holtz, M. E.; Moyer, J. A.; Das, H.; Rébola, A. F.; Heron, J. T.; Clarkson, J. D.; Disseler, S. M.; Liu, Z.; Farhan, A.; Held, R.; Hovden, R.; Padgett, E.; Mao, Q.; Paik, H.; Misra, R.; Kourkoutis, L. F.; Arenholz, E.; Scholl, A.; Borchers, J. A.; Ratcliff, W. D.; Ramesh, R.; Fennie, C. J.; Schiffer, P.; Muller, D. A.; Schlom, D. G. Atomically Engineered Ferroic Layers Yield a Room-Temperature Magnetoelectric Multiferroic. *Nature* **2016**, *537* (7621), 523–527. DOI: 10.1038/nature19343.

(9) Xiao, Z.; Lo Conte, R.; Goiriena-Goikoetxea, M.; Chopdekar, R. V.; Lambert, C.-H. A.; Li, X.; N'Diaye, A. T.; Shafer, P.; Tiwari, S.; Barra, A.; Chavez, A.; Mohanchandra, K. P.; Carman, G. P.; Wang, K. L.; Salahuddin, S.; Arenholz, E.; Bokor, J.; Candler, R. N. Tunable Magnetoelastic Effects in Voltage-Controlled Exchange-Coupled Composite Multiferroic Microstructures. *ACS Appl. Mater. Interfaces* **2020**, *12* (5), 6752–6760. DOI: 10.1021/acsami.9b20876.

(10) Megaw, H. D. Origin of Ferroelectricity in Barium Titanate and Other Perovskite-Type Crystals. *Acta Crystallogr.* **1952**, *5* (6), 739–749. DOI: 10.1107/S0365110X52002069.

(11) Vijatović, M.; Bobić, J.; Stojanović, B. D. History and Challenges of Barium Titanate: Part I. *Sci. Sinter.* **2008**, *40* (2), 155–165. DOI: 10.2298/SOS0802155V.

(12) Gattinoni, C.; Strkalj, N.; Härdi, R.; Fiebig, M.; Trassin, M.; Spaldin, N. A. Interface and Surface Stabilization of the Polarization in Ferroelectric Thin Films. *Proc. Natl. Acad. Sci.* **2020**, *117* (46), 28589–28595. DOI: 10.1073/pnas.2007736117.
(13) Zhang, J.; Zhu, W.; Chen, D.; Qu, H.; Zhou, P.; Popov, M.; Jiang, L.; Cao, L.; Srinivasan, G. Magnetoelectric Effects and Power Conversion Efficiencies in Gyrators with Compositionally-Graded Ferrites and Piezoelectrics. *J. Magn. Magn. Mater.* **2019**, *473*, 131–135. DOI: 10.1016/j.jmmm.2018.10.068.
(14) Channagoudra, G.; Dayal, V. Magnetoelectric Coupling in Ferromagnetic/Ferroelectric Heterostructures: A Survey and Perspective. *J. Alloys Compd.* **2022**, *928*, 167181. DOI: 10.1016/j.jallcom.2022.167181.
(15) Barbier, A.; Mocuta, C.; Stanescu, D.; Jegou, P.; Jedrecy, N.; Magnan, H. Surface Composition of $BaTiO_3/SrTiO_3$ (001) Films Grown by Atomic Oxygen Plasma Assisted Molecular Beam Epitaxy. *J. Appl. Phys.* **2012**, *112* (11), 114116. DOI: 10.1063/1.4768469.
(16) Aghavnian, T.; Moussy, J.-B.; Stanescu, D.; Belkhou, R.; Jedrecy, N.; Magnan, H.; Ohresser, P.; Arrio, M.-A.; Sainctavit, Ph.; Barbier, A. Determination of the Cation Site Distribution of the Spinel in Multiferroic $CoFe_2O_4/BaTiO_3$ Layers by X-Ray Photoelectron Spectroscopy. *J. Electron Spectrosc. Relat. Phenom.* **2015**, *202*, 16–21. DOI: 10.1016/j.elspec.2015.02.006.
(17) Barbier, A.; Aghavnian, T.; Badjeck, V.; Mocuta, C.; Stanescu, D.; Magnan, H.; Rountree, C.; Belkhou, R.; Ohresser, P.; Jedrecy, N. Antiferromagnetic Long-Range Spin Ordering in Fe-and $NiFe_2$-Doped $BaTiO_3$ Multiferroic Layers. *Phys. Rev. B* **2015**, *91* (3), 035417. DOI: 10.1103/PhysRevB.91.035417.
(18) Pangaud, P.; Basolo, S.; Boudet, N.; Berar, J.-F.; Chantepie, B.; Delpierre, P.; Dinkespiler, B.; Hustache, S.; Menouni, M.; Morel, C. XPAD3: A New Photon Counting Chip for X-Ray CT-Scanner. *Nucl. Instrum. Methods Phys. Res. Sect. Accel. Spectrometers Detect. Assoc. Equip.* **2007**, *571* (1), 321–324. DOI: 10.1016/j.nima.2006.10.092.
(19) Medjoubi, K.; Bucaille, T.; Hustache, S.; Bérar, J.-F.; Boudet, N.; Clemens, J.-C.; Delpierre, P.; Dinkespiler, B. Detective Quantum Efficiency, Modulation Transfer Function and Energy Resolution Comparison between CdTe and Silicon Sensors Bump-Bonded to XPAD3S. *J. Synchrotron Radiat.* **2010**, *17* (4), 486–495. DOI: 10.1107/S0909049510013257.
(20) Desjardins, K.; Mocuta, C.; Dawiec, A.; Réguer, S.; Joly, P.; Dubuisson, J.-M.; Alves, F.; Noureddine, A.; Bompard, F.; Thiaudière, D. The CirPAD, a Circular 1.4M Hybrid Pixel Detector Dedicated to X-Ray Diffraction Measurements at Synchrotron SOLEIL. *J. Synchrotron Radiat.* **2022**, *29* (1), 180–193. DOI: 10.1107/S1600577521012492.
(21) Kresse, G.; Hafner, J. Ab Initio Molecular-Dynamics Simulation of the Liquid-Metal--Amorphous-Semiconductor Transition in Germanium. *Phys. Rev. B* **1994**, *49* (20), 14251–14269. DOI: 10.1103/PhysRevB.49.14251.
(22) Kresse, G.; Furthmüller, J. Efficient Iterative Schemes for Ab Initio Total-Energy Calculations Using a Plane-Wave Basis Set. *Phys. Rev. B* **1996**, *54* (16), 11169–11186. DOI: 10.1103/PhysRevB.54.11169.
(23) Blöchl, P. E. Projector Augmented-Wave Method. *Phys. Rev. B* **1994**, *50* (24), 17953–17979. DOI: 10.1103/PhysRevB.50.17953.

(24) Perdew, J. P.; Ruzsinszky, A.; Csonka, G. I.; Vydrov, O. A.; Scuseria, G. E.; Constantin, L. A.; Zhou, X.; Burke, K. Restoring the Density-Gradient Expansion for Exchange in Solids and Surfaces. *Phys. Rev. Lett.* **2008**, *100* (13), 136406. DOI: 10.1103/PhysRevLett.100.136406.
(25) Sharma, K.; Calmels, L.; Li, D.; Barbier, A.; Arras, R. Influence of the Cation Distribution, Atomic Substitution, and Atomic Vacancies on the Physical Properties of $CoFe_2O_4$ and $NiFe_2O_4$ Spinel Ferrites. *Phys. Rev. Mater.* **2022**, *6* (12), 124402. DOI: 10.1103/PhysRevMaterials.6.124402.
(26) Lind, D. M.; Berry, S. D.; Chern, G.; Mathias, H.; Testardi, L. R. Growth and Structural Characterization of Fe_3O_4 and NiO Thin Films and Superlattices Grown by Oxygen-Plasma-Assisted Molecular-Beam Epitaxy. *Phys. Rev. B* **1992**, *45* (4), 1838–1850. DOI: 10.1103/PhysRevB.45.1838.
(27) Rhodes, R. G. Barium Titanate Twinning at Low Temperatures. *Acta Crystallogr.* **1951**, *4* (2), 105–110. DOI: 10.1107/S0365110X51000374.
(28) De Ligny, D.; Richet, P. High-Temperature Heat Capacity and Thermal Expansion of $SrTiO_3$ and $SrZrO_3$ Perovskites. *Phys. Rev. B* **1996**, *53* (6), 3013–3022. DOI: 10.1103/PhysRevB.53.3013.
(29) Venzke, S.; Van Dover, R. B.; Phillips, J. M.; Gyorgy, E. M.; Siegrist, T.; Chen, C.-H.; Werder, D.; Fleming, R. M.; Felder, R. J.; Coleman, E.; Opila, R. Epitaxial Growth and Magnetic Behavior of $NiFe_2O_4$ Thin Films. *J. Mater. Res.* **1996**, *11* (5), 1187–1198. DOI: 10.1557/JMR.1996.0153.
(30) Kim, S.; Seol, D.; Lu, X.; Alexe, M.; Kim, Y. Electrostatic-Free Piezoresponse Force Microscopy. *Sci. Rep.* **2017**, *7* (1), 41657. DOI: 10.1038/srep41657.
(31) Yang, K. J.; Chenming Hu. MOS Capacitance Measurements for High-Leakage Thin Dielectrics. *IEEE Trans. Electron Devices* **1999**, *46* (7), 1500–1501. DOI: 10.1109/16.772500.
(32) Meyer, R.; Waser, R.; Prume, K.; Schmitz, T.; Tiedke, S. Dynamic Leakage Current Compensation in Ferroelectric Thin-Film Capacitor Structures. *Appl. Phys. Lett.* **2005**, *86* (14), 142907. DOI: 10.1063/1.1897425.
(33) Yao, B.; Fang, Z. B.; Zhu, Y. Y.; Ji, T.; He, G. A Model for the Frequency Dispersion of the High- *k* Metal-Oxide-Semiconductor Capacitance in Accumulation. *Appl. Phys. Lett.* **2012**, *100* (22), 222903. DOI: 10.1063/1.4722934.
(34) Lüders, U.; Barthélémy, A.; Bibes, M.; Bouzehouane, K.; Fusil, S.; Jacquet, E.; Contour, J.-P.; Bobo, J.-F.; Fontcuberta, J.; Fert, A. $NiFe_2O_4$: A Versatile Spinel Material Brings New Opportunities for Spintronics. *Adv. Mater.* **2006**, *18* (13), 1733–1736. DOI: 10.1002/adma.200500972.
(35) Fritsch, D.; Ederer, C. Effect of Epitaxial Strain on the Cation Distribution in Spinel Ferrites $CoFe_2O_4$ and $NiFe_2O_4$: A Density Functional Theory Study. *Appl. Phys. Lett.* **2011**, *99* (8), 081916. DOI: 10.1063/1.3631676.
(36) Gil-Monsalve, J.; Martinez-Puente, M. A.; Ostos, C.; Uribe, J. I.; Osorio, J.; Arnache, O. Electronic Structure of Nickel Ferrite Thin Films Growth on Strontium Titanate. *J. Phys. Conf. Ser.* **2021**, *2046* (1), 012061. DOI: 10.1088/1742-6596/2046/1/012061.
(37) Hu, G.; Choi, J. H.; Eom, C. B.; Harris, V. G.; Suzuki, Y. Structural Tuning of the Magnetic Behavior in Spinel-Structure Ferrite Thin Films. *Phys. Rev. B* **2000**, *62* (2), R779–R782. DOI: 10.1103/PhysRevB.62.R779.

(38) Kang, J.-S.; Kim, G.; Lee, H. J.; Kim, D. H.; Kim, H. S.; Shim, J. H.; Lee, S.; Lee, H.; Kim, J.-Y.; Kim, B. H.; Min, B. I. Soft X-Ray Absorption Spectroscopy and Magnetic Circular Dichroism Study of the Valence and Spin States in Spinel Mn Fe 2 O 4. *Phys. Rev. B* **2008**, *77* (3), 035121. DOI: 10.1103/PhysRevB.77.035121.
(39) Stavitski, E.; De Groot, F. M. The CTM4XAS Program for EELS and XAS Spectral Shape Analysis of Transition Metal L Edges. *Micron* **2010**, *41* (7), 687–694. DOI: 10.1016/j.micron.2010.06.005.
(40) Ikeno, H.; de Groot, F. M.; Stavitski, E.; Tanaka, I. Multiplet Calculations of $L_{2,3}$ x-Ray Absorption near-Edge Structures for 3d Transition-Metal Compounds. *J. Phys. Condens. Matter* **2009**, *21* (10), 104208. DOI: 10.1088/0953-8984/21/10/104208.
(41) Tanaka, A.; Jo, T. Resonant 3d, 3p and 3s Photoemission in Transition Metal Oxides Predicted at 2p Threshold. *J. Phys. Soc. Jpn.* **1994**, *63* (7), 2788–2807. DOI: 10.1143/JPSJ.63.2788.
(42) O'Brien, W.; Tonner, B. Orbital and Spin Sum Rules in X-Ray Magnetic Circular Dichroism. *Phys. Rev. B* **1994**, *50* (17), 12672. DOI: 10.1103/PhysRevB.50.12672.
(43) Chen, C.; Idzerda, Y.; Lin, H.-J.; Smith, N.; Meigs, G.; Chaban, E.; Ho, G.; Pellegrin, E.; Sette, F. Experimental Confirmation of the X-Ray Magnetic Circular Dichroism Sum Rules for Iron and Cobalt. *Phys. Rev. Lett.* **1995**, *75* (1), 152. DOI: 10.1103/PhysRevLett.75.152.
(44) Piamonteze, C.; Miedema, P.; De Groot, F. M. F. Accuracy of the Spin Sum Rule in XMCD for the Transition-Metal L Edges from Manganese to Copper. *Phys. Rev. B* **2009**, *80* (18), 184410. DOI: 10.1103/PhysRevB.80.184410.
(45) Nonaka, Y.; Wakabayashi, Y. K.; Shibata, G.; Sakamoto, S.; Ikeda, K.; Chi, Z.; Wan, Y.; Suzuki, M.; Tanaka, A.; Tanaka, M.; Fujimori, A. Origin of Magnetically Dead Layers in Spinel Ferrites MFe_2O_4 Grown on Al_2O_3 : Effects of Postdeposition Annealing Studied by XMCD. *Phys. Rev. Mater.* **2023**, *7* (4), 044413. DOI: 10.1103/PhysRevMaterials.7.044413.
(46) Wakabayashi, Y. K.; Nonaka, Y.; Takeda, Y.; Sakamoto, S.; Ikeda, K.; Chi, Z.; Shibata, G.; Tanaka, A.; Saitoh, Y.; Yamagami, H.; Tanaka, M.; Fujimori, A.; Nakane, R. Cation Distribution and Magnetic Properties in Ultrathin $(Ni_{1-x}Co_x)Fe_2O_4$ (x = 0–1) Layers on Si(111) Studied by Soft x-Ray Magnetic Circular Dichroism. *Phys. Rev. Mater.* **2018**, *2* (10), 104416. DOI: 10.1103/PhysRevMaterials.2.104416.
(47) Hu, Z.; Kaindl, G.; Warda, S. A.; Reinen, D.; de Groot, F. M. F.; Müller, B. G. On the Electronic Structure of Cu(III) and Ni(III) in $La_2Li_{1/2}Cu_{1/2}O_4$, $Nd_2Li_{1/2}Ni_{1/2}O_4$, and Cs_2KCuF_6. *Chem. Phys.* **1998**, *232* (1), 63–74. DOI: 10.1016/S0301-0104(98)00096-2.
(48) Gloter, A.; Ewels, C.; Umek, P.; Arcon, D.; Colliex, C. Electronic Structure of Titania-Based Nanotubes Investigated by EELS Spectroscopy. *Phys. Rev. B* **2009**, *80* (3), 035413. DOI: 10.1103/PhysRevB.80.035413.
(49) Silwal, P.; Miao, L.; Hu, J.; Spinu, L.; Ho Kim, D.; Talbayev, D. Thickness Dependent Structural, Magnetic, and Electronic Properties of the Epitaxial Films of Transparent Conducting Oxide $NiCo_2O_4$. *J. Appl. Phys.* **2013**, *114* (10), 103704. DOI: 10.1063/1.4820930.
(50) Yanagihara, H.; Utsumi, Y.; Niizeki, T.; Inoue, J.; Kita, E. Perpendicular Magnetic Anisotropy in Epitaxially Strained Cobalt-Ferrite (001) Thin Films. *J. Appl. Phys.* **2014**, *115* (17), 17A719. DOI: 10.1063/1.4864048.

(51) Wakabayashi, Y. K.; Nonaka, Y.; Takeda, Y.; Sakamoto, S.; Ikeda, K.; Chi, Z.; Shibata, G.; Tanaka, A.; Saitoh, Y.; Yamagami, H.; Tanaka, M.; Fujimori, A.; Nakane, R. Electronic Structure and Magnetic Properties of Magnetically Dead Layers in Epitaxial $CoFe_2O_4/Al_2O_3/Si(111)$ Films Studied by x-Ray Magnetic Circular Dichroism. *Phys. Rev. B* **2017**, *96* (10), 104410. DOI: 10.1103/PhysRevB.96.104410.
(52) Wisser, J. J.; Emori, S.; Riddiford, L.; Altman, A.; Li, P.; Mahalingam, K.; Urwin, B. T.; Howe, B. M.; Page, M. R.; Grutter, A. J.; Kirby, B. J.; Suzuki, Y. Ultrathin Interfacial Layer with Suppressed Room Temperature Magnetization in Magnesium Aluminum Ferrite Thin Films. *Appl. Phys. Lett.* **2019**, *115* (13), 132404. DOI: 10.1063/1.5111326.
(53) Kaveev, A. K.; Sokolov, N. S.; Suturin, S. M.; Sawada, M.; Voskoboynikov, S. P. High Temperature Treatment of Epitaxial Nickel Ferrite Thin Films: The Way to Bulk-like Magnetic Properties. *J. Cryst. Growth* **2021**, *573*, 126302. DOI: 10.1016/j.jcrysgro.2021.126302.
(54) Miedema, P. S.; de Groot, F. M. F. The Iron L Edges: Fe 2p X-Ray Absorption and Electron Energy Loss Spectroscopy. *J. Electron Spectrosc. Relat. Phenom.* **2013**, *187*, 32–48. DOI: 10.1016/j.elspec.2013.03.005.
(55) Arras, R.; Sharma, K.; Calmels, L. Interplay between Oxygen Vacancies and Cation Ordering in the $NiFe_2O_4$ Spinel Ferrite. *J. Mater. Chem. C* **2024**, *12* (2), 556–561. DOI: 10.1039/D3TC03368F.
(56) Chen, X.; Zhu, X.; Xiao, W.; Liu, G.; Feng, Y. P.; Ding, J.; Li, R.-W. Nanoscale Magnetization Reversal Caused by Electric Field-Induced Ion Migration and Redistribution in Cobalt Ferrite Thin Films. *ACS Nano* **2015**, *9* (4), 4210–4218. DOI: 10.1021/acsnano.5b00456.
(57) Grimaud, A.; May, K. J.; Carlton, C. E.; Lee, Y.-L.; Risch, M.; Hong, W. T.; Zhou, J.; Shao-Horn, Y. Double Perovskites as a Family of Highly Active Catalysts for Oxygen Evolution in Alkaline Solution. *Nat. Commun.* **2013**, *4* (1), 2439. DOI: 10.1038/ncomms3439.
(58) Kalinin, S. V.; Bonnell, D. A. Local Potential and Polarization Screening on Ferroelectric Surfaces. *Phys. Rev. B* **2001**, *63* (12), 125411. DOI: 10.1103/PhysRevB.63.125411.
(59) Lu, H.; Liu, X.; Burton, J. D.; Bark, C.-W.; Wang, Y.; Zhang, Y.; Kim, D. J.; Stamm, A.; Lukashev, P.; Felker, D. A.; Folkman, C. M.; Gao, P.; Rzchowski, M. S.; Pan, X. Q.; Eom, C.-B.; Tsymbal, E. Y.; Gruverman, A. Enhancement of Ferroelectric Polarization Stability by Interface Engineering. *Adv. Mater.* **2012**, *24* (9), 1209–1216. DOI: 10.1002/adma.201104398.
(60) Parker, R.; Lord, H. The Electrical Resistivity of Oxygen Deficient Nickel Ferrite. *Proc. Phys. Soc.* **1959**, *74* (6), 793–795. DOI: 10.1088/0370-1328/74/6/124.
(61) Anjum, S.; Jaffari, G. H.; Rumaiz, A. K.; Rafique, M. S.; Shah, S. I. Role of Vacancies in Transport and Magnetic Properties of Nickel Ferrite Thin Films. *J. Phys. Appl. Phys.* **2010**, *43* (26), 265001. DOI: 10.1088/0022-3727/43/26/265001.
(62) Jedrecy, N.; Aghavnian, T.; Moussy, J.-B.; Magnan, H.; Stanescu, D.; Portier, X.; Arrio, M.-A.; Mocuta, C.; Vlad, A.; Belkhou, R.; Philippe, O.; Barbier, A. Cross-Correlation between Strain, Ferroelectricity, and Ferromagnetism in Epitaxial

Multiferroic $CoFe_2O_4/BaTiO_3$ Heterostructures. *ACS Appl. Mater. Interfaces* **2018**, *10* (33), 28003–28014. DOI: 10.1021/acsami.8b09499.

(63) Margulies, D.; Parker, F.; Rudee, M.; Spada, F.; Chapman, J.; Aitchison, P.; Berkowitz, A. Origin of the Anomalous Magnetic Behavior in Single Crystal Fe 3 O 4 Films. *Phys. Rev. Lett.* **1997**, *79* (25), 5162. DOI: 10.1103/PhysRevLett.79.5162.

(64) Moussy, J.-B.; Gota, S.; Bataille, A.; Guittet, M.-J.; Gautier-Soyer, M.; Delille, F.; Dieny, B.; Ott, F.; Doan, T.; Warin, P.; Bayle-Guillemaud, P.; Gatel, C.; Snoeck, E. Thickness Dependence of Anomalous Magnetic Behavior in Epitaxial Fe_3O_4(111) Thin Films: Effect of Density of Antiphase Boundaries. *Phys. Rev. B* **2004**, *70* (17), 174448. DOI: 10.1103/PhysRevB.70.174448.

(65) Fiévet, F.; Germi, P.; De Bergevin, F.; Figlarz, M. Lattice Parameter, Microstrains and Non-Stoichiometry in NiO. Comparison between Mosaic Microcrystals and Quasi-Perfect Single Microcrystals. *J. Appl. Crystallogr.* **1979**, *12* (4), 387–394. DOI: 10.1107/S0021889879012747.

(66) Cavelius, C.; Moh, K.; Mathur, S. Chemically Designed Growth of Monodisperse Iron Oxide Nanocrystals. *Cryst. Growth Des.* **2012**, *12* (12), 5948–5955. DOI: 10.1021/cg300936t.

(67) Sharona, H.; Loukya, B.; Bhat, U.; Sahu, R.; Vishal, B.; Silwal, P.; Gupta, A.; Datta, R. Coexisting Nanoscale Inverse Spinel and Rock Salt Crystallographic Phases in $NiCo_2O_4$ Epitaxial Thin Films Grown by Pulsed Laser Deposition. *J. Appl. Phys.* **2017**, *122* (22), 225301. DOI: 10.1063/1.4998776.

(68) Tsujie, A.; Hara, Y.; Yanase, T.; Shimada, T.; Nagahama, T. $NiCo_2O_4$ Films Fabricated by Reactive Molecular Beam Epitaxy and Annealing in Various Oxygen Atmospheres. *Appl. Phys. Lett.* **2020**, *116* (23), 232404. DOI: 10.1063/5.0008677.

(69) Kuschel, O.; Buß, R.; Spiess, W.; Schemme, T.; Wöllermann, J.; Balinski, K.; N'Diaye, A. T.; Kuschel, T.; Wollschläger, J.; Kuepper, K. From Fe_3O_4/NiO Bilayers to $NiFe_2O_4$-like Thin Films through Ni Interdiffusion. *Phys. Rev. B* **2016**, *94* (9), 094423. DOI: 10.1103/PhysRevB.94.094423.

(70) Barbier, A.; Belkhou, R.; Ohresser, P.; Gautier-Soyer, M.; Bezencenet, O.; Mulazzi, M.; Guittet, M.-J.; Moussy, J.-B. Electronic and Crystalline Structure, Morphology, and Magnetism of Nanometric Fe_2O_3 Layers Deposited on Pt(111) by Atomic-Oxygen-Assisted Molecular Beam Epitaxy. *Phys. Rev. B* **2005**, *72* (24), 245423. DOI: 10.1103/PhysRevB.72.245423.

For Table of Contents Use Only

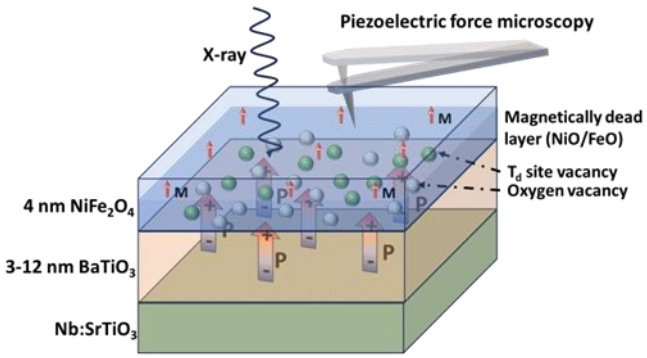

SUPPLEMENTARY INFORMATION

Unveiling and optimizing interface properties of $NiFe_2O_4/BaTiO_3$ heterostructures

Haowen Lin[1,2], Cristian Mocuta[2], Rémi Arras[3], Céline Blaess[1,2], Brice Sarpi[4], Philippe Ohresser[2], Hélène Magnan[1], Jean-Baptiste Moussy[1], Cindy L. Rountree[1], Antoine Barbier[1*]

[1]Université Paris-Saclay, CEA, CNRS, SPEC, 91191, Gif-sur-Yvette, France

[2]Synchrotron SOLEIL, L'Orme des Merisiers Saint-Aubin, BP 48, 91192 Gif sur Yvette Cedex, France

[3]CEMES, Université de Toulouse, CNRS, 29 rue Jeanne Marvig, F-31055 Toulouse, France

[4]Diamond Light Source, Chilton, Didcot, Oxfordshire, UK

1. Topography of epitaxial multilayers

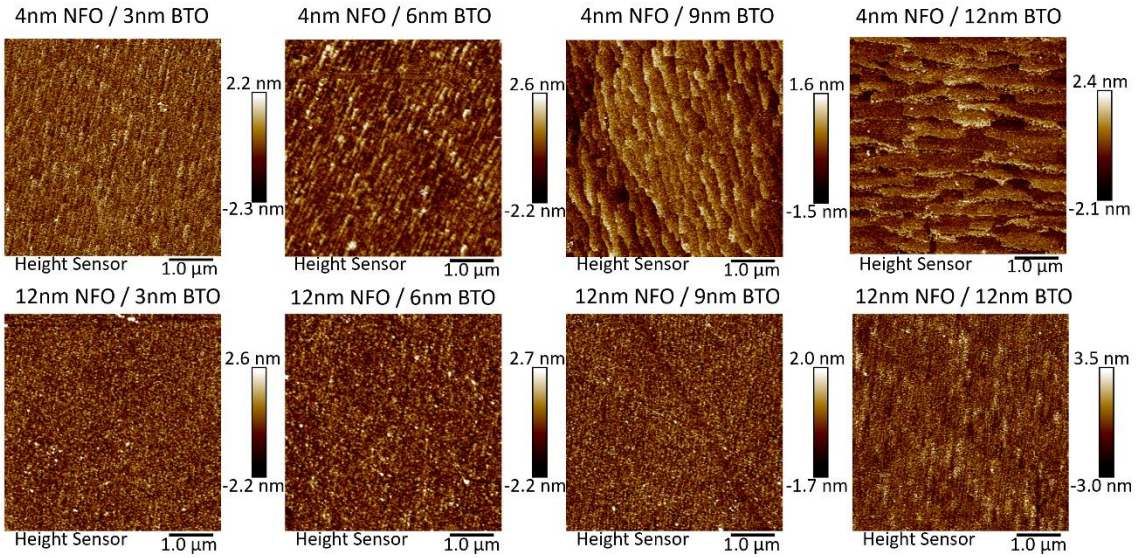

Figure S1: Topography of NFO/BTO multilayers with varying thickness combination, measured by Peak-Force QNM AFM.

2. Reciprocal space mapping for the 12 nm NFO 9 nm BTO film

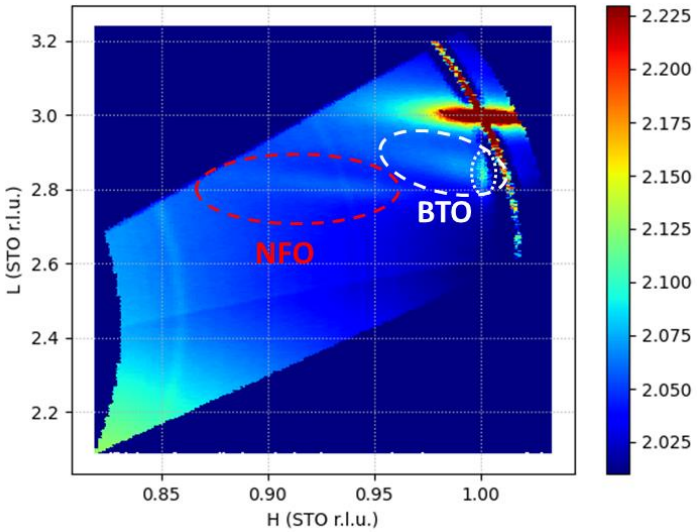

Figure S2: Reciprocal space mapping close to the 113_{STO} reflection for the 12 nm NFO/9 nm BTO sample, with the two coordinates represented in STO reciprocal lattice unit (r.l.u.).

3. PFM written patterns and corresponding written voltage on the samples

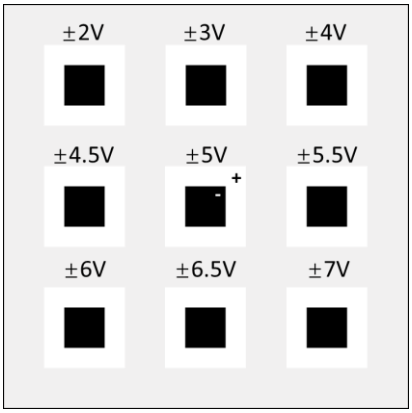

Figure S3: Illustration of PFM written patterns and corresponding written voltages.

4. PFM amplitude and phase curves

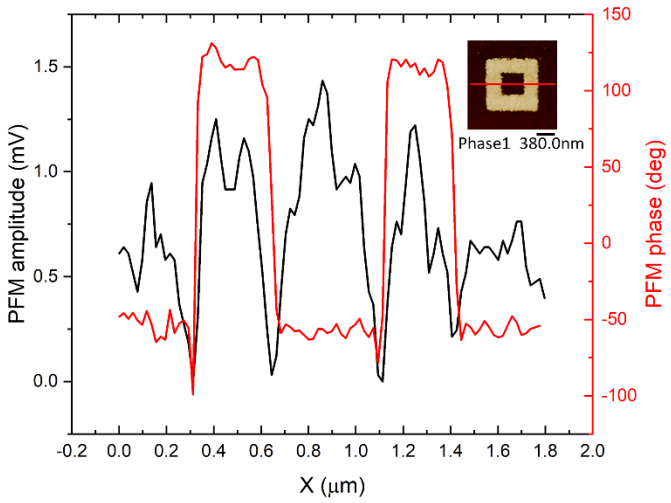

Figure S4. PFM amplitude and phase curves recorded during scanning the lateral position of the square-in-square pattern on the sample (red line in the inset).

5. Magnetic hysteresis loop for as-deposited and vacuum-annealed samples

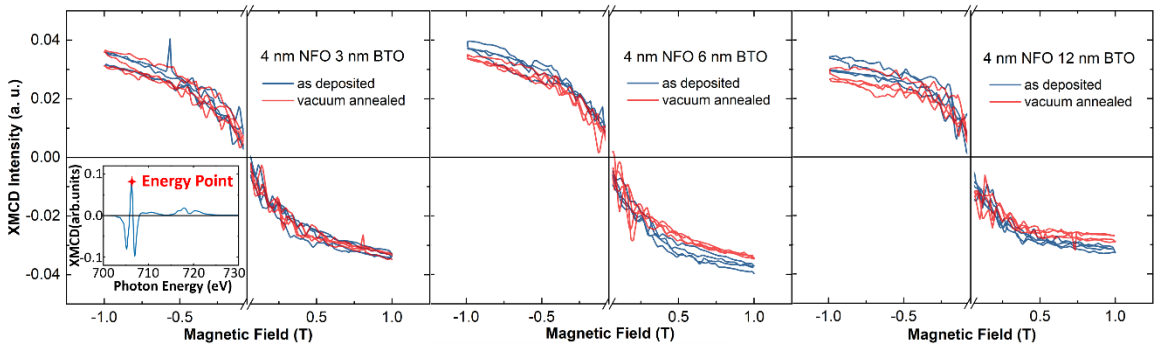

Figure S5. Magnetic hysteresis loop based on normalized XMCD intensity acquired at X-ray energy of 706.26eV (corresponding to the middle peak of the XMCD curve of Fe L_3 edge) for as-deposited samples (blue line) and vacuum annealed samples (red line) with increasing BTO thickness (from left to right). The inset in the first image is an XMCD spectrum to illustrate the energy point used to the hysteresis loop, marked by a red star.

6. Calculation of inversion parameter in spinel $NiFe_2O_4$

As formerly specified in the main text, the chemical formula of a mixed spinel structure $NiFe_2O_4$ is written as

$$\left[\mathrm{Ni}_{1-y}\mathrm{Fe}_{y}\right]_{\mathrm{Td}}\left[\mathrm{Ni}_{y}\mathrm{Fe}_{2-y}\right]_{\mathrm{Oh}}\mathrm{O}_4 \tag{S1}$$

Here, y is the inversion parameter. Due to the presence of Fe^{3+}_{Oh}, Fe^{2+}_{Oh} and Fe^{3+}_{Td} in the system, we can thus write an equation to obtain inversion parameter y from the proportion between iron ions in Oh and Td site:

$$\frac{2-y}{y} = \frac{x(\mathrm{Fe}^{3+}_{\mathrm{Oh}}) + x(\mathrm{Fe}^{2+}_{\mathrm{Oh}})}{x(\mathrm{Fe}^{3+}_{\mathrm{Td}})} \tag{S2}$$

$$\frac{2}{y} = \frac{x(\mathrm{Fe}^{3+}_{\mathrm{Oh}}) + x(\mathrm{Fe}^{2+}_{\mathrm{Oh}})}{x(\mathrm{Fe}^{3+}_{\mathrm{Td}})} + 1 \tag{S3}$$

$$y = \frac{2}{\frac{x(\mathrm{Fe}^{3+}_{\mathrm{Oh}}) + x(\mathrm{Fe}^{2+}_{\mathrm{Oh}})}{x(\mathrm{Fe}^{3+}_{\mathrm{Td}})} + 1} = 2 * x(\mathrm{Fe}^{3+}_{\mathrm{Td}}) \tag{S4}$$

Here, $x(\mathrm{Fe}^{3+}_{\mathrm{Oh}})$, $x(\mathrm{Fe}^{2+}_{\mathrm{Oh}})$, and $x(\mathrm{Fe}^{3+}_{\mathrm{Td}})$ are the percentage of Fe^{3+}_{Oh}, Fe^{2+}_{Oh} and Fe^{3+}_{Td} in all the Fe ions of mixed spinel structure NFO, respectively.

7. Calculation of T_d vacancies in spinel structure

In inverse spinel, one Fe is occupying O_h site and one Fe is occupying T_d site per NFO f.u., rendering the ratio between Fe ions in T_d and O_h sites 1:1. Normally, as the structure transfer from inverse to direct, Fe ions in T_d site will transfer to O_h site with Ni transferring from O_h to T_d. Here, however, with Fe^{3+} leaving the T_d sites, Ni stays at O_h sites, making no available O_h sites to accommodate the Fe^{3+} ions leaving from T_d. As a result, the amount of Fe ions in O_h site remains the same, but the amount of Fe ions in T_d sites decreases. By calculating the deviation from the 1:1 ratio, we can thus obtain the proportion of T_d vacancies in T_d sites, $x\left(\mathrm{Fe}^{3+}_{\mathrm{Td}}\ \mathrm{vacancies}\right)$ as:

$$\frac{1 - x\left(\mathrm{Fe}^{3+}_{\mathrm{Td}}\mathrm{vacancies}\right)}{1} = \frac{x\left(\mathrm{Fe}^{3+}_{\mathrm{Td}}\right)}{x(\mathrm{Fe}_{\mathrm{Oh}})} \tag{S5}$$

$$x\left(\mathrm{Fe}^{3+}_{\mathrm{Td}}\ \mathrm{vacancies}\right) = 1 - \frac{x\left(\mathrm{Fe}^{3+}_{\mathrm{Td}}\right)}{x(\mathrm{Fe}_{\mathrm{Oh}})} \tag{S6}$$

Here, $x(\mathrm{Fe}_{\mathrm{Oh}})$ and $x(\mathrm{Fe}^{3+}_{\mathrm{Td}})$ are the percentage $\mathrm{Fe}_{\mathrm{Oh}}$ (both Fe^{3+}_{Oh} and Fe^{2+}_{Oh} sites) and Fe^{3+}_{Td} in all the Fe ions of mixed spinel structure NFO, respectively.

8. Evolution of magnetic moments of each type of Fe ions for as-deposited and vacuum-annealed samples

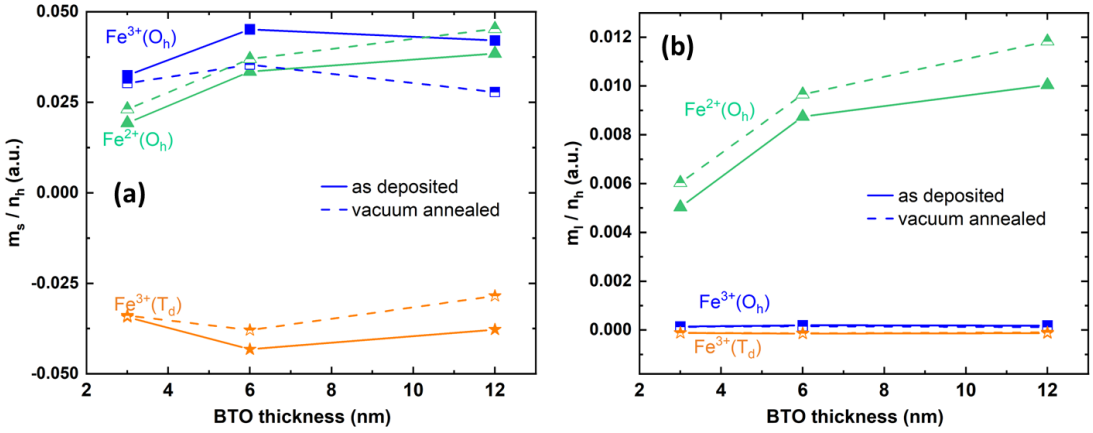

Figure S6. Evolution of magnetic moments of each type of Fe ions *versus* θ_{BTO} for samples in as-deposited and vacuum-annealed states. Panel (a) and (b) represent the evolution of spin and orbital magnetic moments, respectively. The solid lines denote that the sample is in as-deposited state, while the dashed lines refer to vacuum annealed state.

9. Comparison between experimental and calculated XMCD spectrum near Ni $L_{3,2}$ edge

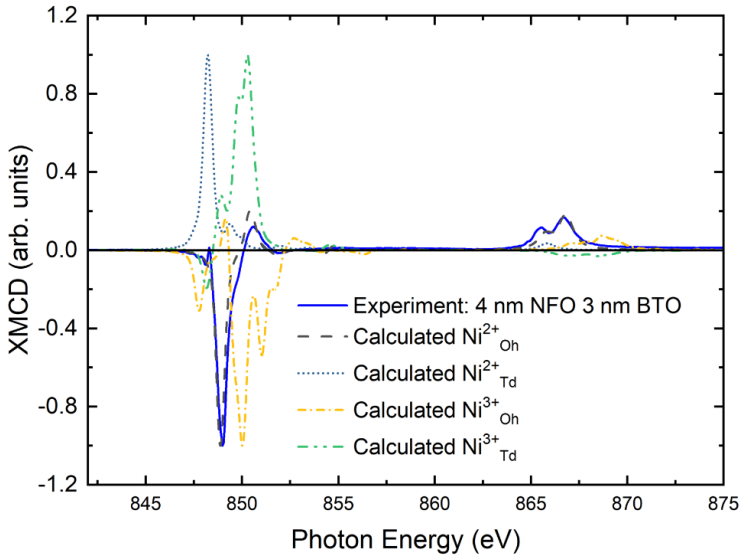

Figure S7. Experimental and calculated XMCD spectra near Ni $L_{3,2}$ edge. Solid line represents the experimental spectrum of a 4 nm NFO/3 nm BTO sample. Other lines in dash or dots represents the calculated XMCD spectra at the $L_{3,2}$ edge for Ni^{2+}_{Oh}, Ni^{2+}_{Td}, Ni^{3+}_{Oh} and Ni^{3+}_{Td} sites. The experiment spectrum is very similar to calculated Ni^{2+}_{Oh} spectrum and does not comprehend other calculated spectra of Ni^{2+}_{Td}, Ni^{3+}_{Oh} and Ni^{3+}_{Td} sites.

9. Normalized XMCD spectra for as-deposited and air-annealed samples

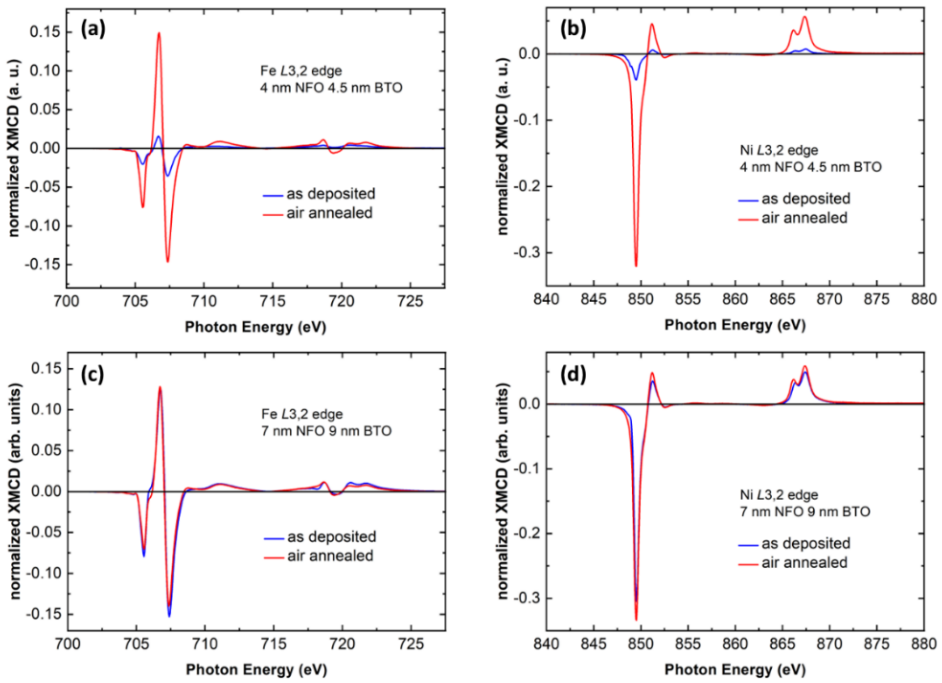

Figure S8. Normalized experimental XMCD spectra for as-deposited and air-annealed samples. Panels (a) and (b) display the XMCD spectra near the Fe $L_{3,2}$ and Ni $L_{3,2}$ edges, respectively, for the 4 nm NFO/4.5 nm BTO sample. Panels (c) and (d) similarly present the spectra near the Fe $L_{3,2}$ and Ni $L_{3,2}$ edges for the 7 nm NFO/9 nm BTO sample.

10. Magnetic hysteresis loop for as-deposited and air-annealed samples

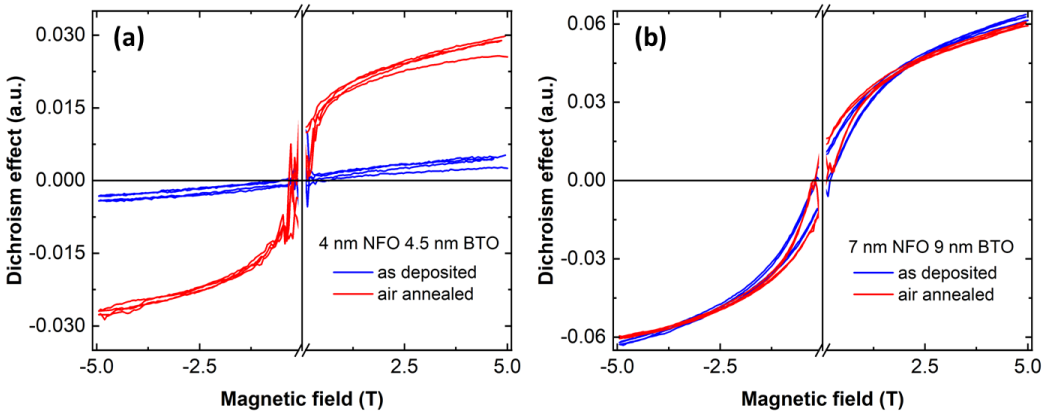

Figure S9. Magnetic hysteresis loop based on normalized XMCD intensity acquired at X-ray energy of 706.73 eV (corresponding to the middle peak of the XMCD curve of Fe L_3 edge) for as-deposited samples (blue line) and air annealed samples (red line). Panels (a) and (b) represents the hysteresis loop of the 4 nm NFO/4.5 nm BTO sample and 7 nm NFO/9 nm BTO sample, respectively.

11. Evolution of magnetic moments of each type of Fe ions for as-deposited and air-annealed samples

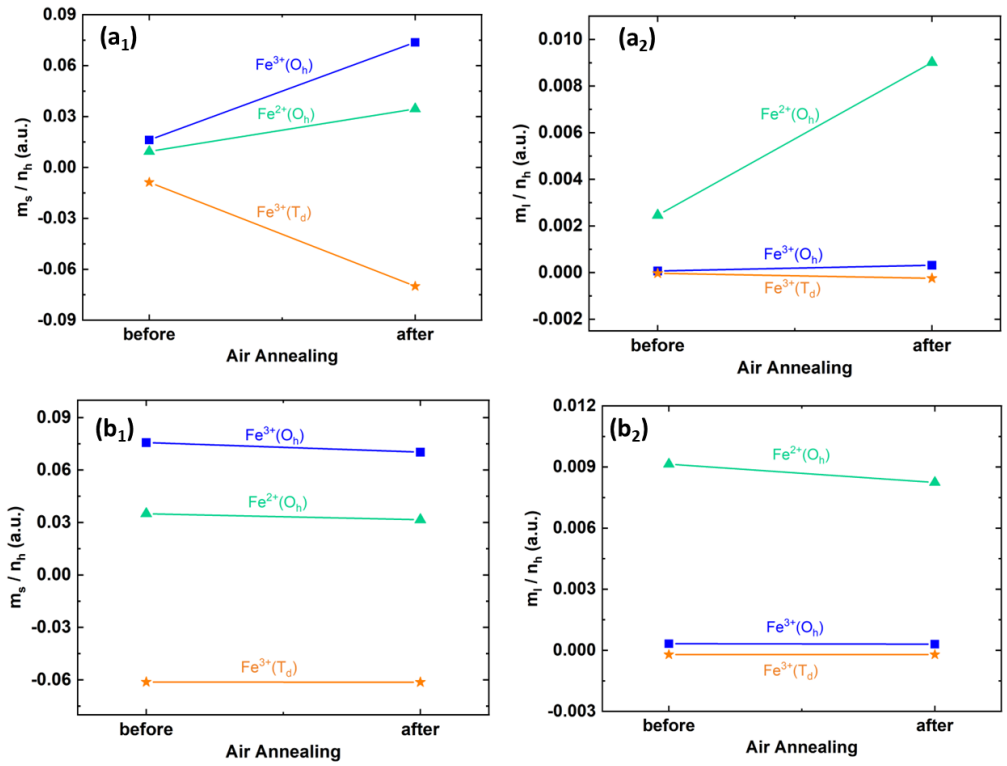

Figure S10. Evolution of magnetic moments of each type of Fe ions for samples in as-deposited and air-annealed status. Panels (a_1) and (a_2) represents the evolution of spin and orbital magnetic moments, respectively, for the 4 nm NFO/4.5 nm BTO sample. Panels (b_1) and (b_2) similarly present the evolution of spin and orbital magnetic moments for the 7 nm NFO/9 nm BTO sample.

12. Percentage of tetrahedral (T_d) site vacancies for as-deposited, air-annealed, and vacuum-annealed samples

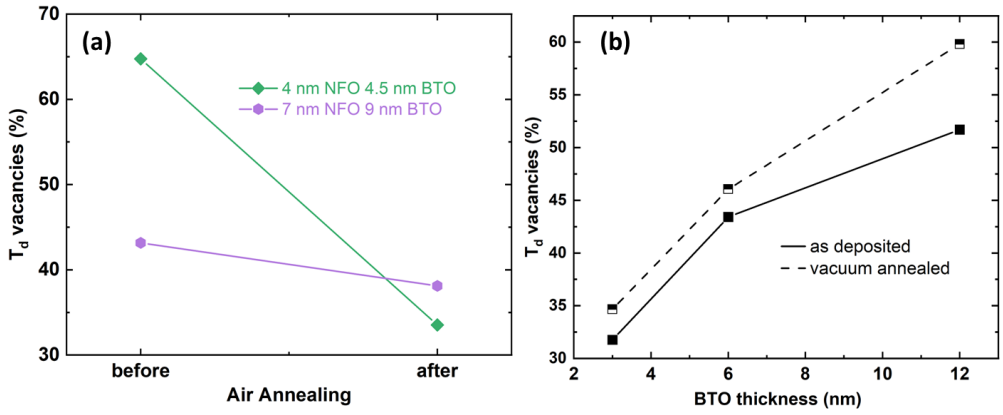

Figure S11. Evolution of tetrahedral (T_d) site vacancies for as-deposited, air-annealed, and vacuum-annealed samples. (a) Evolution of T_d vacancies before and after air annealing for 4 nm NFO/4.5 nm BTO sample (green line) and 7 nm NFO/9 nm BTO sample (purple line). (b) Evolution of Td vacancies *versus* θ_{BTO} for as deposited and vacuum annealed state of the three 4 nm - NFO samples with 3, 6 and 12 nm of BTO.